Author Manuscript:
Published in final edited form as: *Surf. Interface Anal.* Volume 47, Issue 9, Pages 871-888, September 2015. https://doi.org/10.1002/sia.5789

Calculations of electron inelastic mean free paths. X. Data for 41 elemental solids over the 50 eV to 200 keV range with the relativistic full Penn algorithm

H. Shinotsuka,[1*] S. Tanuma,[1†] C. J. Powell,[2] and D. R. Penn[2]

[1]National Institute for Materials Science, 1-2-1 Sengen, Tsukuba, Ibaraki 305-0047, Japan
[2]National Institute of Standards and Technology, Gaithersburg, MD 20899, USA

ABSTRACT

We have calculated inelastic mean free paths (IMFPs) for 41 elemental solids (Li, Be, graphite, diamond, glassy C, Na, Mg, Al, Si, K, Sc, Ti, V, Cr, Fe, Co, Ni, Cu, Ge, Y, Nb, Mo, Ru, Rh, Pd, Ag, In, Sn, Cs, Gd, Tb, Dy, Hf, Ta, W, Re, Os, Ir, Pt, Au, and Bi) for electron energies from 50 eV to 200 keV. The IMFPs were calculated from measured energy loss functions for each solid with a relativistic version of the full Penn algorithm. The calculated IMFPs could be fitted to a modified form of the relativistic Bethe equation for inelastic scattering of electrons in matter for energies from 50 eV to 200 keV. The average root-mean-square (RMS) deviation in these fits was 0.68 %. The IMFPs were also compared with IMFPs from a relativistic version of our predictive TPP-2M equation that was developed from a modified form of the relativistic Bethe equation. In these comparisons, the average RMS deviation was 11.9 % for energies between 50 eV and 200 keV. This RMS deviation is almost the same as that found previously in a similar comparison for the 50 eV to 30 keV range (12.3 %). Relatively large RMS deviations were found for diamond, graphite, and cesium as in our previous comparisons. If these three elements were excluded in the comparisons, the average RMS deviation was 8.9 % between 50 eV and 200 keV. The relativistic TPP-2M equation can thus be used to estimate IMFPs in solid materials for energies between 50 eV and 200 keV. We found satisfactory agreement between our calculated IMFPs and those from recent calculations and from measurements at energies of 100 keV and 200 keV.

[*] Present address: Advanced Algorithm & Systems, Co. Ltd., Ebisu IS Bldg. 7F, Ebisu 1-13-6, Shibuya, Tokyo 150-0013, Japan
[†] Corresponding Author; tanuma.shigeo@nims.go.jp

Author Manuscript:
Published in final edited form as: *Surf. Interface Anal.* Volume 47, Issue 9, Pages 871-888, September 2015. https://doi.org/10.1002/sia.5789

Introduction

The inelastic mean free path (IMFP) is a fundamental parameter in surface electron spectroscopies such as X-ray photoelectron spectroscopy (XPS) and Auger-electron spectroscopy (AES) for many applications[1,2]. We have previously reported IMFP calculations for 27 elemental solids, 15 inorganic compounds, and 14 organic compounds at electron energies between 50 eV and 2 keV[3,4,5,6,7]. We also developed a predictive IMFP equation, designated TPP-2M, that can be used to estimate IMFPs in other materials [1,2,4,5]. In recent years, there has been growing interest in XPS and related experiments using X-rays with energies of up to about 15 keV for both scientific and industrial purposes [6,7]. We therefore calculated IMFPs for electron energies up to 30 keV, and results have been published for 41 elemental solids [8]. In this work, we found that the TPP-2M equation was useful for energies between 50 eV and 30 keV [8]. Since there is a need for IMFPs in transmission electron microscopy (TEM) [9], we now report IMFP calculations for energies up to 200 keV.

Our IMFP calculations were made with the Penn algorithm [10]. With this algorithm, the probability of inelastic scattering as a function of energy loss is determined from experimental energy-loss functions (ELFs) for each material while the probability of inelastic scattering as a function of momentum transfer is determined from the Lindhard dielectric model [11]. For our work in which we calculated IMFPs for electron energies between 50 eV and some higher energy (2 keV or 30 keV), we used what we term the full Penn algorithm (FPA) for energies up to either 200 eV [4,5,6,7] or 300 eV [8] that involves triple integrations as described in the next section. For higher energies, we used a simpler version of the Penn algorithm, the so-called single-pole approximation (SPA) that involves only a single integration. At 300 eV, the differences between IMFPs from the FPA and the SPA were very small (e.g., < 0.2 % for graphite) [8].

We previously reported IMFPs for 41 elemental solids at energies between 50 eV and 30 keV [8]. Unfortunately, these calculations were made with a non-relativistic formalism. The relativistic corrections to the electron energy are 1.4 %, 2.9 %, 5.6 %, and 8.2 % at energies of 5 keV, 10 keV, 20 keV, and 30 keV, respectively [9]. In this paper, we report IMFP calculations using a relativistic version of the FPA for 41 elemental solids (Li, Be, graphite, diamond, glassy carbon, Na, Mg, Al, Si, K, Sc, Ti, V, Cr, Fe, Co, Ni, Cu, Ge, Y, Nb, Mo, Ru, Rh, Pd, Ag, In, Sn, Cs, Gd, Tb, Dy, Hf, Ta, W, Re, Os, Ir, Pt, Au, and Bi). These calculations were made using experimental ELFs for electron energies from 50 eV to 200 keV. We also describe the algorithm for the relativistic IMFP calculations and the analysis of these IMFPs with relativistic Fano plots. Finally, we compare our calculated IMFPs with the IMFPs calculated by Fernandez-Varea *et al.* [12] and with the IMFPs measured by Iakoubovskii *et al.* [13], McCartney *et al.*[14], and Wang *et al.*[15].

IMFP Calculations with the Relativistic Full Penn Algorithm

We utilize the relativistic full Penn algorithm (FPA) to calculate IMFPs for energies in the 50 eV to 200 keV range in order to be consistent with our previous stopping power calculations[16]. IMFPs were calculated at equal energy intervals on a logarithmic scale

Author Manuscript:
Published in final edited form as: *Surf. Interface Anal.* Volume 47, Issue 9, Pages 871-888, September 2015. https://doi.org/10.1002/sia.5789

corresponding to increments of 10 % from 10 eV to 1 MeV. We present IMFPs for energies between 10 eV and 50 eV and between 200 keV and 1 MeV in Figures but these results are shown only to illustrate trends.

As for our previous IMFP calculations[8], we made use of measured ELFs or experimental optical data to determine ELFs (the "optical" ELFs). IMFPs were calculated with the FPA using a model ELF (here the Lindhard dielectric function[11]) where the dependence of the model ELF on energy loss is the same as the dependence of the experimental ELF on energy loss[10]. This calculation involves triple integrations over plasmon energy ω_p, momentum transfer q, and energy loss ω [10]. In our previous papers [3,4,5,6,7,8], we calculated IMFPs with integrations first on q and then on ω and ω_p. In this paper, we calculate IMFPs from the probability $p(T,\omega)$ for energy loss ω per unit distance traveled by an electron with electron kinetic energy T. Our calculation now has integrations first on ω_p and then on q and ω. This method could also be applied easily in our related relativistic stopping power calculations with the FPA.[16] We used Hartree atomic units ($m_e = e = \hbar = 1$) in our calculations, where m_e is the electron rest mass, e is the elementary charge, and $\hbar$ is the reduced Planck constant.

The relativistic differential cross section (DCS) for inelastic scattering can be expressed as the sum of a longitudinal DCS, $d^2\sigma_L/d\omega dq$, and a transverse DCS, $d^2\sigma_T/d\omega dq$. Since the transverse DCS can be neglected for electron energies less than about 0.5 MeV[16,17], the relativistic inelastic DCS can then be written as [12]

$$\frac{d^2\sigma}{d\omega dq} = \frac{d^2\sigma_L}{d\omega dq} + \frac{d^2\sigma_T}{d\omega dq} \approx \frac{d^2\sigma_L}{d\omega dq} \approx \frac{2}{\pi N v^2}\,\mathrm{Im}\left(\frac{-1}{\varepsilon(q,\omega)}\right)\frac{1}{q} \qquad (1)$$

where N is the number of atoms per unit volume, v is the electron velocity, $\mathrm{Im}\left[-1/\varepsilon(q,\omega)\right]$ is the model ELF, and $\varepsilon(q,\omega)$ is the complex dielectric function. With the Penn algorithm [10], the energy dependence of the model ELF can be obtained from the measured ELF for each material while the dependence of the ELF on q can be obtained from the Lindhard model dielectric function[11].

The probability $p(T,\omega)$ for energy loss ω per unit distance traveled by an electron with kinetic energy T with respect to the Fermi level can be calculated from Eqn (1):

$$p(T,\omega) = \frac{2}{\pi v^2}\int_{q_-}^{q_+}\frac{dq}{q}\,\mathrm{Im}\left[\frac{-1}{\varepsilon(q,\omega)}\right] = \frac{\left(1+T'/c^2\right)^2}{1+T'/\left(2c^2\right)}\frac{1}{\pi T'}\int_{q_-}^{q_+}\frac{dq}{q}\,\mathrm{Im}\left[\frac{-1}{\varepsilon(q,\omega)}\right] \qquad (2)$$

where, $T' = T + E_f$, $q_\pm = \sqrt{T'\left(2+T'/c^2\right)} \pm \sqrt{\left(T'-\omega\right)\left(2+\left(T'-\omega\right)/c^2\right)}$, E_f is the Fermi energy, and c is the speed of light. The IMFP, λ, can be calculated from Eqn (2) with the following equation:

Author Manuscript:
Published in final edited form as: *Surf. Interface Anal.* Volume 47, Issue 9, Pages 871-888, September 2015. https://doi.org/10.1002/sia.5789

$$\lambda(T) = \left[\int_0^{\omega_{\max}} p(T,\omega)\, d\omega\right]^{-1} \tag{3}$$

where $\omega_{\max} = T' - E_f$.

The ELF in the FPA model can be expressed as:

$$\mathrm{Im}\left[\frac{-1}{\varepsilon(q,\omega)}\right] = \int_0^{\infty} d\omega_p g(\omega_p)\,\mathrm{Im}\left[\frac{-1}{\varepsilon^L(q,\omega;\omega_p)}\right] \tag{4}$$

where ε^L denotes the Lindhard model dielectric function of a free electron gas with plasmon energy $\omega_p \left(=\sqrt{4\pi n}\right)$, n is the electron density, $g(\omega_p)$ is a coefficient introduced to satisfy the condition $\mathrm{Im}[-1/\varepsilon(q=0,\omega)] = \mathrm{Im}[-1/\varepsilon(\omega)]$, and $\mathrm{Im}[-1/\varepsilon(\omega)]$ is the optical or measured ELF. The coefficient $g(\omega_p)$ is then given by

$$g(\omega) = \frac{2}{\pi\omega}\mathrm{Im}\left[\frac{-1}{\varepsilon(\omega)}\right] \tag{5}$$

The energy-loss function from the FPA in Eqn (4) can be described as the sum of two contributions, one associated with the plasmon pole and the other with single-electron excitations:

$$\mathrm{Im}\left[\frac{-1}{\varepsilon(q,\omega)}\right] = \mathrm{Im}\left[\frac{-1}{\varepsilon(q,\omega)}\right]_{pl} + \mathrm{Im}\left[\frac{-1}{\varepsilon(q,\omega)}\right]_{se} \tag{6}$$

The plasmon-pole contribution can be expressed as

$$\mathrm{Im}\left[\frac{-1}{\varepsilon(q,\omega)}\right]_{pl} = g(\omega_0)\frac{\pi}{\left|\partial\varepsilon_1^L(q,\omega,\omega_p)/\partial\omega_p\right|_{\omega_p=\omega_0}}\theta\left(q^-(\omega;\omega_0) - q\right), \tag{7}$$

$$q^{\pm}(\omega;\omega_p) = \pm k_F(\omega_p) + \sqrt{k_F^2(\omega_p) + 2\omega} \tag{8}$$

$$k_F = (3\pi/4)^{1/3}\omega_p^{2/3} \tag{9}$$

where ω_0 is a numerical solution that satisfies $\varepsilon_1^L(q,\omega;\omega_0) = 0$ and $\theta(x)$ is the step function. The derivative of $\varepsilon_1^L(q,\omega,\omega_p)$ with respect to ω_p is

$$\frac{\partial\varepsilon_1^L(q,\omega,\omega_p)}{\partial\omega_p} = \frac{1}{3\pi\omega_p q z^2}\left\{\ln\left|\frac{Y_- + 1}{Y_- - 1}\right| + \ln\left|\frac{Y_+ + 1}{Y_+ - 1}\right|\right\} \tag{9}$$

Author Manuscript:
Published in final edited form as: *Surf. Interface Anal.* Volume 47, Issue 9, Pages 871-888, September 2015. https://doi.org/10.1002/sia.5789

where $Y_{\pm} \equiv z \pm \frac{1}{4}\left(\frac{z}{x}\right)^{-1}$, $x = \omega / E_F$, $z = q / 2k_F$, $E_F = k_F^2 / 2$ is the Fermi energy, and k_F is the Fermi wave vector corresponding to a given ω_p as shown in Eqn (9). To reduce numerical errors in the calculation at the limiting cases when $z/x < 0.01$ and $z/x > 100$, we use the following approximate equations:

$$\ln\left|\frac{Y_- + 1}{Y_- - 1}\right| + \ln\left|\frac{Y_+ + 1}{Y_+ - 1}\right| \approx -\frac{64}{3} z a^2 \left\{3 + 48(1+z^2)a^2 + 256(3+z^2)(1+3z^2)a^4\right\}, \quad (10)$$

where $a \equiv z/x$ when $z/x < 0.01$, and

$$\ln\left|\frac{Y_- + 1}{Y_- - 1}\right| + \ln\left|\frac{Y_+ + 1}{Y_+ - 1}\right| \approx \ln\left(\frac{z+1}{z-1}\right)^2 + 4zb^2\left\{1 + (1+z^2)b^2 + \frac{1}{3}(3+z^2)(1+3z^2)b^4\right\}, \quad (11)$$

where $b \equiv x/(z(z^2-1))$ when $z/x > 100$.

The contribution of single-electron excitations can be described as:

$$\mathrm{Im}\left[\frac{-1}{\varepsilon(q,\omega)}\right]_{se} = \int_0^\infty d\omega_p g(\omega_p) \mathrm{Im}\left[\frac{-1}{\varepsilon^L(q,\omega;\omega_p)}\right] \theta\left(q^+(\omega,\omega_p) - q\right)\theta\left(q - q^-(\omega,\omega_p)\right). \quad (12)$$

where the real and imaginary parts of the Lindhard dielectric function, ε_1^L and ε_2^L, are

$$\varepsilon_1^L = 1 + \frac{1}{\pi k_F z^2}\left[\frac{1}{2} + \frac{1}{8z}\left\{F\left(z - \frac{x}{4z}\right) + F\left(z + \frac{x}{4z}\right)\right\}\right] \quad (13)$$

and

$$\varepsilon_2^L = \frac{1}{8k_F z^3} \times \begin{cases} x & \text{for } 0 < x < 4z(1-z) \\ 1 - (z - x/4z)^2 & \text{for } |4z(1-z)| < x < 4z(1+z) \\ 0 & \text{otherwise} \end{cases} \quad (14)$$

where $F(t) = (1-t^2)\ln|(t+1)/(t-1)|$. To reduce numerical errors in the calculations at the limiting conditions $u \equiv \omega/qk_F << 1$ and $u >> z+1$, ε_1^L and ε_2^L can be calculated from

$$\varepsilon_1^L = 1 + \frac{2}{\pi q z}\left(\frac{1}{2} + \frac{1}{4z}\left[(1 - z^2 - u^2)\ln\left|\frac{z+1}{z-1}\right| + (z^2 - u^2 - 1)\frac{2u^2 z}{(z^2-1)^2}\right]\right),$$
$$\varepsilon_2^L = \frac{u}{qz}. \quad (15)$$

when $u << 1$ and

$$\varepsilon_1^L = 1 - \frac{\omega_p^2}{\omega^2}\left\{1 + \left(z^2 + \frac{3}{5}\right)\frac{1}{u^2}\right\},$$
$$\varepsilon_2^L = 0. \quad (16)$$

Author Manuscript:
Published in final edited form as: *Surf. Interface Anal.* Volume 47, Issue 9, Pages 871-888, September 2015. https://doi.org/10.1002/sia.5789

when $u >> z+1$.

The material-property data used in the IMFP calculations and in the analysis of ELFs and IMFPs were the same as in our previous publication[8]. For that work, the ELFs of our 41 elemental solids were extended only up to energy losses of 30 keV. In the present study, we require ELFs for energy losses up to 1 MeV. ELFs for energy losses between 30 keV and 1 MeV were calculated from atomic photoabsorption data or atomic scattering factors [18].

We checked the internal consistency of the ELF data with the oscillator-strength sum rule (or f-sum rule) and a limiting form of the Kramers-Kronig integral (or KK-sum rule).[5, 19] The f-sum can be evaluated as the total effective number of electrons per atom, Z_{eff}, contributing to the inelastic scattering:

$$Z_{eff} = (2/\pi\hbar^2\Omega_p^2)\int_0^{\Delta E_{\max}} \Delta E\,\mathrm{Im}[-1/\varepsilon(\Delta E)]d(\Delta E) \qquad (17)$$

where $\Delta E = \hbar\omega$, $\Omega_p = (4\pi n_a e^2/m)^{1/2}$, $n_a = N_a\rho/M$ is the density of atoms, N_{a} is Avogadro's number, ρ is the mass density, and M is the atomic weight. The maximum energy loss in Eqn (18), $\Delta E_{\max}$, was 1 MeV.

Table 1 shows values of Z_{eff} from Eqn (18) for the 41 elemental solids where we see reasonable agreement between the atomic number, Z, of the solid and Z_{eff} calculated from our ELF data. The percentage differences between Z_{eff} and Z are less than 5 % except for Mg, K, Sc, Cr, Fe, Nb, Ag, and Cs where the differences are less than 11 %. For all 41 solids, the root-mean-square (RMS) percentage difference between Z_{eff} and Z was 4.2 %. We found the same result previously where $\Delta E_{\max}$ was chosen to be 30 keV (the maximum energy for our earlier IMFP calculations) and where we made a correction for the contributions of K-shell excitations that were not included in the Z_{eff} integration for Z ≥ 50 [8]. We found the same average RMS error for the KK-sum rule integrations as before, 7.7 %, because the KK-sum integrations saturate for energy losses over 1 keV [8].

Results

Calculated IMFPs from the relativistic Full Penn Algorithm

Table 2 shows our calculated IMFPs for the 41 elemental solids as a function of the electron kinetic energy, T, with respect to the Fermi energy between 50 eV and 200 keV. Plots of the calculated IMFPs as a function of electron energy are shown as solid circles in Figs. 1 to 8. IMFPs are included in these plots for energies less than 50 eV and over 200 keV to illustrate trends. The IMFPs for energies less than 50 eV, however, are not considered as reliable as those at higher energies [8, 20] while the IMFPs for energies larger than 200 keV must be slightly larger than the correct values because we neglected the contribution of the transverse DCS shown in Eqn (1).

The plots of calculated IMFPs in Figs. 1 to 8 show similar dependences on electron energy for energies over 200 eV for all of the solids. For energies less than 200 eV, however, there are appreciable variations in the shapes of the plots (i.e., the positions and the shapes of

the minima) that are due to different shapes of the ELFs for each material [21]. For energies over 50 keV, the slopes of the IMFP *vs*. electron energy plots become smaller than those for energies between about 1 keV and 30 keV; these slope changes must be due to relativistic effects.

Comparison of IMFPs from present and previous calculation procedures

We now examine the differences, Δ, between IMFPs from our present calculation procedure, λ_{new}, as shown in Table 2 for each of the 41 elemental solids and the corresponding IMFPs from our previous procedure [8], λ_{old}. Figures 9, 10, and 11 show plots of Δ for each element as a function of energy between 50 eV and 500 eV. These differences arise mainly from changes in our interpolation procedures, as detailed below. We also changed the integration order for ω_p, q, and ω in the FPA calculations, as described in the section "IMFP Calculations with the Relativistic Full Penn Algorithm", but tests with model ELF functions showed that this change did not significantly affect the IMFP results.

In the present FPA calculation procedure, we first performed linear interpolations on the ELFs at $q = 0$ for elemental solids in order to obtain the "full" ELFs at $q > 0$ as shown in Eqn (4), which should have a sufficient number of finite energy steps or grids for the ω_p, q, and ω integrations. The interpolation grids for ω_p were automatically determined so that the integration in Eqn (13) converged satisfactorily with use of the Romberg-Simpson method. Next, two-dimensional interpolation grids in the (q, ω) plane were automatically determined so that the whole integration in Eqn (3) converged at all electron energies by use of the adaptive-integration method with the Simpson formula. The resulting two-dimensional grids had irregular intervals. Those grids were then interpolated properly to obtain $p(T, \omega)$ in Eqn (2) and the $\lambda(T)$ in Eqn (3) at each electron energy, where the cubic-spline integration method was applied.

In our previous work [8], we did not use any interpolations in the ELF. The q and ω integrals of the ELF were performed using the Gaussian quadrature formula. The final integration over ω_p was needed only for the FPA calculations. The changes in the numerical-calculation procedures described here must be responsible for the small differences between λ_{new} and λ_{old} in Figs. 9 to 11. We also note that we used the SPA for energies over 300 eV in our previous calculations. As a result, there are small discontinuities in the difference plots of Figs. 9 to 11.

The IMFP differences in Figs. 9 to 11 are positive for energies less than 300 eV except for glassy carbon at around 200 eV, Sn at around 50 eV, and Au at around 50 eV. The IMFP differences for these three solids, however, are only slightly negative. This result means that the new calculation procedure with the FPA mostly gave larger IMFPs than those found previously with the FPA [8]. Nevertheless, the IMFP differences in Figs. 9 to 11 are generally small, with the largest about 0.05 nm for Nb and Ag at about 80 eV. We also see relatively large differences, around 0.03 nm, for Cs at energies between 200 eV and 300 eV. Because the IMFPs for Cs are larger than for the other elements (except K) for energies over 50 eV and have a slightly different energy dependence, as shown in Fig. 6, it is reasonable to see relatively large IMFP differences for Cs in Fig. 11. The relative differences of the new to old Cs IMFPs,

however, are less than 2 % for energies between 50 eV and 500 eV. The different shapes and magnitudes of the difference plots in Figs. 9 to 11 are believed to be associated with the different shapes of the ELFs for each solid.

For energies between 300 eV and 500 eV, we found negative differences between λ_{new} and λ_{old} for Li (Fig. 9), K (Fig. 9), and Y (Fig. 10). These negative differences are believed to be mainly due to use of the FPA algorithm in the present IMFP calculations. As mentioned earlier, we used the SPA for energies over 300 eV in our previous work [8].

Figure 12 shows plots of the averages of the absolute differences, λ_{new} - λ_{old}, for our 41 elemental solids as a function of electron energy, again for energies between 50 eV and 500 eV. These average differences are less than 0.02 nm for energies less than 300 eV and less than 0.01 nm for energies between 300 eV and 500 eV. We also show the RMS percentage differences that are less than 5 % for energies between 50 eV and 350 eV and less than 1 % for higher energies. Our new IMFPs are believed to be more reliable than our previous IMFPs [8] since we used more appropriate and thus more reliable interpolations in the ELF calculations with the FPA for $q \neq 0$ in our triple-integral calculations.

Relativistic modified Bethe equation

We earlier proposed a predictive IMFP equation, designated TPP-2M, that could be used to estimate IMFPs in different materials [6]:

$$\lambda = \frac{E}{E_p^2[\beta_{nr}\ln(\gamma_{nr}E) - (C_{nr}/E) + (D_{nr}/E^2)]} \tag{18}$$

where E is the non-relativistic kinetic energy (with respect to the Fermi level) and β_{nr}, γ_{nr}, C_{nr}, and D_{nr} are parameters. Equation (19) was based on our early IMFP calculations for a group of 27 elemental solids [4] and a group of 14 organic compounds [6]. The form of Eqn (19) was developed based on the non-relativistic Bethe equation [22] for the total cross section for inelastic scattering, $\sigma_{tot}^{non-rel}$, by atoms [23]:

$$\sigma_{tot}^{non-rel} = \frac{4\pi a_0^2}{(E/R)}\left[M_{tot}^2 \ln\left(\frac{4c_{tot}E}{R}\right) + \frac{\gamma_{tot}}{(E/R)} + O\left(\frac{R^2}{E^2}\right)\right] \tag{19}$$

and the definition $n_a\lambda\sigma_{tot} = 1$. In Eqn (20), R is the Rydberg energy (13.605 eV), a_0 is the Bohr radius (52.918 pm), M_{tot}^2 is the square of the dipole matrix element for all possible inelastic-scattering processes, c_{tot} and γ_{tot} are parameters, and O represents the next high-order term in the asymptotic expansion for the Bethe equation.

The relativistic expression for the total inelastic cross section, σ_{tot}^{rel} is [23]

Author Manuscript:
Published in final edited form as: *Surf. Interface Anal.* Volume 47, Issue 9, Pages 871-888, September 2015. https://doi.org/10.1002/sia.5789

$$\sigma_{tot}^{rel} = \frac{8\pi a_0^{\,2}}{m_e v^2 / R}\left\{ M_{tot}^{\,2}\left[\ln\left(\frac{\beta^2}{1-\beta^2} \right) - \beta^2 \right] + C_{tot} \right\} \tag{20}$$

where $\beta = v/c$, c is the speed of light, and

$$C_{tot} = M_{tot}^{\,2}\left[\ln c_{tot} + \ln\left(2m_e c^2 / R\right) \right] = M_{tot}^{\,2}\left[\ln c_{tot} + 11.2268 \right] \tag{21}$$

Equation (21) can be rewritten in the same form as Eq. (20):

$$\sigma_{tot}^{rel} = \frac{4\pi a_0^{\,2}}{m_e v^2 / 2R}\left\{ M_{tot}^{\,2}\left[\ln\left(\frac{4c_{tot}}{R}\frac{m_e v^2}{2} \right) - \ln\left(1-\beta^2\right) - \beta^2 \right] \right\} \tag{22}$$

The corresponding IMFP is:

$$\lambda = \frac{m_e v^2 / 2}{E_p^2 \beta_r \left[\ln\left(\gamma_r m_e v^2 / 2\right) - \ln(1-\beta^2) - \beta^2 \right]} \tag{23}$$

where β_r, γ_r, C_r, and D_r are new parameters analogous to β_{nr}, γ_{nr}, C_{nr}, and D_{nr} in Eqn (19). For energies less than 200 eV, the terms in $1/E$ and $1/E^2$ in Eq. (19) become important [4] . We then obtain the following general IMFP expression to represent the relativistic Bethe equation that is modified to be useful for energies from 50 eV to 200 keV:

$$\lambda_F = \frac{\alpha(T)T}{E_p^2\left\{\beta_r\left[\ln(\gamma_r \alpha(T)T) - \ln(1-\beta^2) - \beta^2\right] - (C_r/T) + (D_r/T^2)\right\}} \tag{24}$$

where $\alpha(T)T = m_e v^2/2$ and $\alpha(T) = \frac{1+T/(2m_e c^2)}{\left[1+T/(m_e c^2)\right]^2} \approx \frac{1+T/1021999.8}{(1+T/510998.9)^2}$.

We have chosen the upper energy limit of 200 keV for use of Eqn (25) because this was the

Author Manuscript:
Published in final edited form as: *Surf. Interface Anal.* Volume 47, Issue 9, Pages 871-888, September 2015. https://doi.org/10.1002/sia.5789

upper-energy limit of our IMFP results in Table 2.

The β terms in the denominator of Eqn (25) are very small and must be negligible for energies less than 30 keV. We then obtain the following simpler and more approximate equation:

$$\lambda_s = \frac{\alpha(T)T}{E_p^2\left\{\beta_r\left[\ln(\gamma_r\alpha(T)T)\right]-(C_r/T)+(D_r/T^2)\right\}} \qquad (25)$$

For energies over 10 keV, the C_r and D_r terms in Eqns (25) and (26) are negligible. The ratio of IMFPs from Eqns (26) and (25) is then

$$\lambda_S/\lambda_F = \frac{\ln(\gamma_r\alpha(T)T)-\ln(1-\beta^2)-\beta^2}{\ln(\gamma_r\alpha(T)T)} \qquad (26)$$

This IMFP ratio depends on the electron energy T and on values of the parameter γ_r for each solid. We will see shortly that values of γ_r for our 41 solids are nearly the same (within 13 %) as the values of γ_{nr} found previously for nonrelativistic energies between 50 eV and 30 keV [8]. The latter values are in the range 0.04 eV^{-1} to 0.5 eV^{-1} for our 41 elemental solids. The IMFP ratios from Eqn (27) are then ≤1.001 at 30 keV, ≤1.007 at 100 keV, ≤1.020 at 200 keV, and ≤1.054 at 500 keV. We conclude that it is satisfactory to use the simpler Eqn (26) for further analyses of our calculated IMFPs for energies up to 200 keV. We will then present our new values of γ_r.

Relativistic TPP-2M equation

Our goal here is to develop a relativistic version of the TPP-2M equation [Eqn (19)] based on the new IMFPs for 41 elemental solids in Table 2. As in our previous work with lower electron energies [4-8], we use Fano plots [24] to analyze the energy dependence of IMFPs for each solid for energies between 50 eV and 200 keV. These plots were made by plotting $\alpha(T)T/\lambda$ *vs.* $\ln(\alpha(T)T)$, as suggested by Eqn (26). The IMFPs for each element were also fitted with Eqn (26) to derive values of the parameters β_r, γ_r, C_r, and D_r shown in Table 3. As just noted, the values of γ_r in Table 3 are close (within 13 %) to the values of γ_{nr} found previously for nonrelativistic energies between 50 eV and 30 keV [8], and our use of Eqn (26) for the fits is justified. We also determined the root-mean-square percentage deviation, *RMS*, between IMFPs from the fit, $\lambda_{fit}(T_i)$ with respect to the calculated IMFPs, $\lambda(T_i)$ in Table 2:

$$RMS = 100\times\left[\sum_{i=1}^{n}\left(\frac{\lambda_{fit}(T_i)-\lambda(T_i)}{\lambda(T_i)}\right)^2\Big/n\right]^{0.5} \qquad (\%) \qquad (27)$$

Author Manuscript:
Published in final edited form as: *Surf. Interface Anal.* Volume 47, Issue 9, Pages 871-888, September 2015. https://doi.org/10.1002/sia.5789

where n = 83 is the number of electron energies in Table 2. Values of *RMS* for each solid are shown in Table 3. These values range from 0.25 % (for graphite) to 1.26 % (for Co), while the average value of *RMS* for the 41 elements was 0.68 %. Equation (26) is thus a convenient analytical representation of the calculated IMFPs (e.g., for interpolation).

Figure 13 shows representative Fano plots for Al, Cu, and Au where the solid circles represent the calculated IMFPs from the relativistic FPA, as shown in Table 2, and the open circles show results of similar calculations for energies up to 1 MeV. The solid and dashed lines show curve-fit results with Eqns (26) and (25), respectively, that were performed for energies between 50 eV and 200 keV. We see that both Eqns (25) and (26) provide good fits to the calculated IMFPs with RMS deviations of 0.98%, 1.41%, and 0.59% with Eqn (25) and slightly smaller RMS deviations of 0.82%, 1.24%, and 0.47% with Eqn (26) for Al, Cu, and Au, respectively. We conclude that both Eqns (25) and (26) provide satisfactory fits to the calculated IMFPs of Al, Cu, and Au for energies between 50 eV and 200 keV.

Figure 13 also shows extrapolations of the solid and dashed lines for energies up to 1 MeV to show the trends of these equations. The simpler and more approximate Eqn (26) (solid lines) does happen to agree well with the calculated IMFPs for Al, Cu, and Ag. Nevertheless, we know that the differences between IMFPs from Eqns (25) and (26) must be due to the β terms in Eqn (25) that were neglected in Eqn (26). That is, these β terms need to be considered in Fano plots for energies over 200 keV. For such energies, Fano plots should be made by plotting $\alpha(T)T/\lambda$ versus $\ln\left(\alpha(T)T\right)-\ln\left(1-\beta^2\right)-\beta^2$ or, equivalently, $\alpha(T)T/\lambda$ versus $\ln[\beta^2/(1-\beta^2)]-\beta^2$ as suggested by Eqn (21). These Fano plots would be expected to be linear for relativistic energies. Our present IMFP calculations neglected the contributions of transverse contributions to the DCS in Eqn (1) that would increase the total inelastic-scattering cross sections and decrease the IMFPs. We therefore expect that Eqn (25) should better represent IMFPs than Eqn (26) for energies larger than 200 keV.

We have chosen to use the simpler Eqn (26) for fitting our calculated IMFPs and for our Fano plots because it has the same form as the non-relativistic TPP-2M equation [Eqn (19)] that we developed earlier for estimating IMFPs in materials [6]. This equation was based on an analysis of IMFPs that had been calculated from optical data for electron energies between 50 eV and 2000 eV. These IMFP calculations had been performed with the non-relativistic FPA (for energies less than 300 eV) and the SPA (for energies over 330 eV). Simple expressions were found for the four parameters in Eqn (19) in terms of material properties:

$$\beta_{nr} = -1.0 + 9.44/\left(E_p^2 + E_g^2\right)^{0.5} + 0.69\rho^{0.1} \qquad (\mathrm{eV^{-1}nm^{-1}}) \tag{29a}$$

$$\gamma_{nr} = 0.191\rho^{-0.5} \qquad (\mathrm{eV^{-1}}) \tag{29b}$$

$$C_{nr} = 19.7 - 9.1U \quad (\mathrm{nm^{-1}}) \tag{29c}$$

$$D_{nr} = 534 - 208U \quad (\mathrm{eVnm^{-1}}) \tag{29d}$$

Author Manuscript:
Published in final edited form as: *Surf. Interface Anal.* Volume 47, Issue 9, Pages 871-888, September 2015. https://doi.org/10.1002/sia.5789

$$U = \frac{N_v \rho}{M} = \left(E_p / 28.816 \right)^2 \tag{29e}$$

where E_p is the free-electron plasmon energy (in eV), E_g is the bandgap energy for nonconductors (in eV), N_v is the number of valence electrons [25] per atom or molecule, M is the atomic or molecular weight, and ρ is expressed in [g cm^{-3}].

Equations (25) and (29) or Eqns (26) and (29) represent two alternative forms of our relativistic TPP-2M formula for estimating IMFPs in materials. That is, $\beta_r = \beta_{nr}$, $\gamma_r = \gamma_{nr}$, $C_r = C_{nr}$, and $D_r = D_{nr}$. IMFPs calculated from Eqns (26) and (29), were already shown in Figs. 1 to 8 as dashed lines for each elemental solid, and Table 4 shows the RMS deviations between these IMFPs and the corresponding IMFPs calculated from optical data with the relativistic FPA (as shown in Table 2). Table 4 also shows the RMS deviations between IMFPs from Eqns (25) and (29) and the corresponding calculated IMFPs for each solid. We see that the RMS deviations from use of Eqns (25) and (26) are almost identical, with individual differences ≤ 0.3 %.

The average RMS deviation between IMFPs from Eqns (26) and (29) and the corresponding calculated IMFPs for the 41 elemental solids over the 50 eV to 200 keV range was 11.9 %. The same average RMS deviation was obtained when Eqns (25) and (29) were used to estimate IMFPs. These average RMS deviations are almost the same as those found in similar comparisons for the 50 eV to 2000 eV range (12.8 %) and for the 50 eV to 30 keV range (12.3 %) [8]. Although there is generally excellent agreement between IMFPs from our relativistic TPP-2M equation [Eqns (26) and (29)] and the corresponding optical IMFPs in Figs. 1 to 8 for energies between 50 eV and 200 keV, there are significant disagreements for graphite, diamond, and cesium for which the RMS deviations from Table 4 are 46.6 %, 70.7 %, and 34.7 %, respectively. Possible reasons for these large disagreements were discussed in earlier papers [7, 8]. If the RMS deviations for these three solids are ignored, the average RMS deviation for the remaining elements is 8.9 %. This value is almost the same as that found in a similar analysis for the 50 eV to 30 keV range (9.2 %) [8]. We note here that our IMFP results for our other elemental solids are based on ELF data for polycrystalline samples and that the magnitudes of possible allotrope effects remain to be explored.

Figure 14 shows plots of ratios of IMFPs calculated from the relativistic TPP-2M equation [Eqns (26) and (29)] to IMFPs calculated from optical data for the 41 elemental solids as a function of electron energy in order to assess visually the reliability of the TPP-2M equation for energies up to 200 keV. Ideally, these ratios should not change with energy and should be close to unity. The ratios in Fig. 14 are nearly constant for energies between 300 eV and 200 keV but there are often substantial changes at lower energies. A detailed discussion of the changes in the ratios for energies less than 30 keV was given in a previous paper[8]. We conclude that the relativistic TPP-2M formula consisting of Eqns (26) and (29) can be used for estimation of IMFPs in solid materials for energies between 50 eV and 200 keV.

Discussion

We make comparisons here of our calculated IMFPs with recent IMFP calculations by Fernandez-Varea *et al.*[12] for energies up to 1 MeV and with IMFP measurements from transmission electron microscopy (TEM) experiments at 100 keV and 200 keV [13-15].

Comparisons of IMFPs with other calculated IMFPs

Fernandez-Varea *et al.*[12] calculated IMFPs for Al, Si, Cu, and Au for energies from 10 eV to 1 MeV using a relativistic optical-data model that included both longitudinal and transverse contributions to the DCS. The generalized oscillator strength (GOS) in their model was obtained from a semi-empirical optical oscillator strength (OOS) density with an algorithm that extended the OOS to non-zero momentum transfers. Figure 15 shows comparisons of these IMFPs (solid squares) with our optical IMFPs (solid circles) and IMFPs from the simplified relativistic TPP-2M equations [Eqns (26) and (29)] (solid lines) for energies between 10 eV and 200 keV. We note here that we had shown the equivalence of the alternate forms of the TPP-2M equation, Eqns (25) and (26), for energies less than 200 keV in Fig. 13. As for Figs. 1 to 8, we show our optical IMFPs between 10 eV and 50 eV to indicate trends although these results are not as reliable as those for higher energies. For Al and Si, we see a generally high degree of consistency between our IMFPs and those of Fernandez-Varea *et al.* We also see good consistency of our IMFPs for Cu and Au with those of Fernandez-Varea *et al.* for energies above 500 eV. Small but systematic differences occur at lower energies. These differences must be due to differences of the ELFs used in each calculation or to the different dispersion relations that were used in each calculation. We also see good agreement between the IMFPs of Fernandez-Varea *et al.* for Al, Si, Cu, and Au and those from the relativistic TPP-2M equation for energies over 200 eV.

Figure 16 shows comparisons of our IMFPs for Al, Si, Cu, and Au, the IMFPs of Fernandez-Varea *et al.*[12], and IMFPs from the more exact relativistic TPP-2M equation [Eqns (25) and (29)] for energies between 100 keV and 1 MeV. We see generally increasing differences between our IMFPs and those of Fernandez-Varea *et al.* with increasing energy (although the differences for Al are relatively small). As noted earlier in connection with Fig. 13, our IMFPs are expected to be larger than those of Fernandez-Varea *et al.* for energies over about 200 keV because of our neglect of the contributions of transverse interactions to the DCS in Eqn (1) [12]. Our relativistic TPP-2M equation shows the same trends with increasing energy as the Fernandez-Varea et al. IMFPs due to the β terms in Eqn (25).

Comparisons of IMFPs with measured IMFPs

A number of IMFP measurements have been made by TEM at electron energies of 100 keV or 200 keV [9,13-15]. Most of these measurements were made by analyses of the electron energy-loss spectrum (EELS), typically over an energy-loss range of about 150 eV, as described by Egerton [9]. The ratio of the IMFP to the thin-film specimen thickness can be determined from the natural logarithm of the EELS intensity divided by the intensity for the no-loss peak. The IMFP can then be obtained if the specimen thickness is known. Alternatively, the specimen thickness can be calculated from a Kramers-Kronig transform of the EELS spectrum [13]. Two

groups have determined IMFPs by off-axis electron holography [14,15]. The uncertainties of IMFPs from the EELS experiments and from the holography experiments have been estimated to be about 10 % but intercomparisons of IMFPs from different laboratories suggest that the uncertainties could be up to about 25 % [9].

Iakoubovskii *et al*. [13] determined IMFPs from EELS experiments at 200 keV for 47 elemental solids and 42 inorganic compounds. Egerton [9] lists IMFPs obtained from EELS measurements at 100 keV for 11 elemental solids (Be, an arc-evaporated carbon film, diamond, Al, Si, Cr, Fe, Cu, Ag, Hf, and Au). McCartney *et al*. [14] and Wang *et al*. [15] reported IMFPs derived from their electron-holography experiments for Si at 100 keV and for Cu at 200 keV, respectively. We have already compared our calculated IMFPs with these measured IMFPs that were shown as symbols in Figs. 1 to 8 for 32 elemental solids (Be, glassy carbon, diamond, Mg, Al, Si, Ti, V, Cr, Fe, Co, Ni, Cu, Ge, Y, Nb, Mo, Ru, Pd, Ag, In, Sn, Gd, Dy, Hf, Ta, W, Re, Ir, Pt, Au, and Bi). In general, we see good agreement between our calculated IMFPs and the measured IMFPs for the 32 solids. We note, however, that the measured IMFPs vary greatly from a minimum IMFP of 56 nm for Au at 100 keV to a maximum IMFP of 160 nm for Be at 200 keV.

Figure 17 shows a plot of our calculated IMFPs for the 32 elemental solids at 100 keV and 200 keV (from the results in Table 2 and with interpolations using Eqn (26) and the parameters in Table 3) versus the corresponding measured IMFPs at energies of 100 keV and 200 keV. We see an excellent correlation between the calculated and measured IMFPs at both electron energies except for Be which shows relatively large differences (-36 % at 100 keV and -21 % at 200 keV). These systematic differences for Be indicate either that the calculated IMFPs are too low (with respect to the trend of the measurements indicated by the solid line in Fig. 17) or that the measured IMFPs for Be are too large (with respect to the correlation line in Fig. 17). These differences could be due to oxidation of the Be films used in the TEM experiments or of the Be films and surfaces used to determine the optical constants from which we calculated the Be ELF [7]. Although our Be ELF satisfied key sum-rule checks [7], Arakawa *et al*. comment that variability in the reported optical constants of Be is likely due to the difficulty of Be sample preparation [26].

The average RMS differences between the calculated and measured IMFPs in Fig. 17 are 18.5 % at 100 keV (for 11 elemental solids, 12 measurements) and 11.2 % at 200 keV (for 32 elemental solids). If Be is excluded from this comparison because of the large systematic offsets in Fig. 17, the average RMS differences are 15.9 % at 100 keV and 10.8 % at 200 keV. The overall average RMS difference between the calculated IMFPs and the measured IMFPs at both 100 keV and 200 keV was 13.6 % with inclusion of the Be results and 12.3 % with the exclusion of Be in the comparisons. The latter average RMS differences are comparable to the estimated uncertainty of about 10 % for the IMFP measurements. We also note that the average RMS differences of the calculated and measured IMFPs in Fig. 17 are similar to those found in comparisons [8] of IMFPs calculated from optical data with IMFPs obtained from elastic-peak electron-spectroscopy (EPES) experiments.[27, 28, 29] These comparisons showed RMS differences of 12 % for a group of 11 elemental solids and energies

Author Manuscript:
Published in final edited form as: *Surf. Interface Anal.* Volume 47, Issue 9, Pages 871-888, September 2015. https://doi.org/10.1002/sia.5789

between 100 eV and 5 keV and of 15 % for a group of 17 elemental solids and energies between 300 eV and 3.4 keV [8].

Figure 18 shows comparisons of IMFPs calculated from the relativistic TPP-2M equation [Eqns (26) and (29)] with IMFPs measured at 100 keV and 200 keV for the same 32 elemental solids. In general, we see a satisfactory correlation between the IMFPs from the TPP-2M equation and the measured IMFPs. However, we see relatively large deviations (greater than 30 %) for Hf (33 %) at 100 keV, and diamond (49 %), Y (32 %) and In (32 %) at 200 keV. The average RMS differences between IMFPs from the TPP-2M equation and the measured IMFPs are 18.5 % at 100 keV and 16.9 % at 200 keV, with an overall average RMS deviation of 17.4 % for both energies. This average RMS difference is also almost the same as in similar comparisons of IMFPs from the TPP-2M equation and IMFPs measured by EPES, 11 % for a group of 11 elemental solids with measurements between 100 eV and 5 keV and 19 % for a group of 17 elemental solids with measurements between 300 eV and 3.4 keV [8].

Summary

We report new calculations of IMFPs for 41 elemental solids (Li, Be, graphite, diamond, glassy C, Na, Mg, Al, Si, K, Sc, Ti, V, Cr, Fe, Co, Ni, Cu, Ge, Y, Nb, Mo, Ru, Rh, Pd, Ag, In, Sn, Cs, Gd, Tb, Dy, Hf, Ta, W, Re, Os, Ir, Pt, Au, and Bi) for electron energies from 50 eV to 200 keV. The IMFPs were calculated from experimental optical data using the probability $p(T,\omega)$ for energy loss ω per unit distance traveled by an electron with relativistic kinetic energy T with the relativistic full Penn algorithm for energies up to 200 keV.

The calculated IMFPs could be fitted with a modification of the relativistic Bethe equation for inelastic scattering of electrons in matter for energies between 50 eV and 200 keV. The average RMS deviation in these fits was 0.68 %. We also developed a relativistic version of our TPP-2M equation [Eqns (26) and (29)] that could be used to estimate IMFPs for electron energies between 50 eV and 200 keV. This predictive IMFP equation is based on the modified relativistic Bethe equation. The four parameters in the relativistic TPP-2M equation are calculated using the same equations that were developed for our original TPP-2M equation. The latter equation was based on our earlier IMFP calculations for a group of 27 elemental solids and a group of 14 organic compounds with electron energies between 50 eV and 2 keV [6].

We compared our calculated IMFPs with values from the relativistic TPP-2M equation and found an average RMS deviation of 11.9 % for the 41 solids; this average RMS deviation was almost the same as that found in a previous comparison for the 50 eV to 30 keV range (12.3 %). Large RMS deviations were found for diamond, graphite, and cesium (70.7 %, 46.6 %, and 34.7 %, respectively) as shown in Table 4; possible reasons for these large deviations were discussed in a previous paper [8]. If the RMS deviations for diamond, graphite, and cesium are excluded, the average RMS deviation for the remaining 38 elements was 8.9 %. This value is slightly superior to the corresponding average RMS deviation of 9.2 % found with IMFPs for the 50 eV to 30 keV range for the same elements [8] and 10.2 % for the 50 eV to 2 keV range for our original group of 27 elemental solids [6]. We therefore believe that the

Author Manuscript:
Published in final edited form as: *Surf. Interface Anal.* Volume 47, Issue 9, Pages 871-888, September 2015. https://doi.org/10.1002/sia.5789

relativistic TPP-2M equation should be useful for estimating IMFPs in most materials for electron energies between 50 eV and 200 keV with an average RMS uncertainty of about 10 %. Nevertheless, we point out that possible allotropic effects remain to be examined.

We compared our calculated IMFPs with those from recent calculations and experiments. Our calculated IMFPs for Al and Si and energies between 10 eV and 200 keV agree well with those of Fernandez-Varea *et al*. [12] that were calculated from a relativistic optical-data model. There is similar good agreement between our IMFPs for Cu and Au and those of Fernandez-Varea *et al*. for energies between 500 eV and 200 keV. There are small but systematic differences at lower energies that must be due to differences of the optical energy-loss functions or to the different dispersion relations that were used in each IMFP algorithm.

We also compared our calculated IMFPs with measured IMFPs from TEM experiments at 100 keV for 11 elemental solids and at 200 keV for 32 elemental solids. We found satisfactory agreement in these comparisons with an overall average RMS difference between them of 13.6 % (or 12.3 % with the exclusion of Be in the comparisons). These average RMS differences are similar to the estimated uncertainty of about 10 % for the IMFP measurements. We also compared IMFPs from the relativistic TPP-2M equation proposed in the present work with the IMFPs determined from TEM experiments. We again found good agreement in these comparisons except for Hf at 100 keV and diamond, Y, and In at 200 keV. The average RMS difference between IMFPs from the TPP-2M equation and the measured IMFPs is 17.4 %.

Author Manuscript:
Published in final edited form as: *Surf. Interface Anal.* Volume 47, Issue 9, Pages 871-888, September 2015. https://doi.org/10.1002/sia.5789

References

[1] C. J. Powell, A. Jablonski, *Nucl. Instrum. Meth. Phys. Res. A* **2005** ; 601, 54.

[2] C. J. Powell, A. Jablonski, *J. Electron Spectrosc. Relat. Phenom.* **2010** ; 178-179, 331.

[3] S. Tanuma, C. J. Powell, D. R. Penn, *Surf. Interface Anal.* **1988** ; 11, 577.

[4] S. Tanuma, C. J. Powell, D. R. Penn, *Surf. Interface Anal.* **1991** ; 17, 911.

[5] S. Tanuma, C. J. Powell, D. R. Penn, *Surf. Interface Anal.* **1991** ; 17, 927.

[6] S. Tanuma, C. J. Powell, D. R. Penn, *Surf. Interface Anal.* **1994** ; 21, 165.

[7] S. Tanuma, C. J. Powell, D. R. Penn, *Surf. Interface Anal.* **2005** ; 37, 1.

[8] S. Tanuma, C. J. Powell, D. R. Penn, *Surf. Interface Anal.* **2011** ; 43, 689.

[9] R. F. Egerton, *Electron Energy-Loss Spectroscopy in the Electron Microscope*, third edition, Springer, New York, **2011**.

[10] D. R. Penn, *Phys. Rev. B* **1987** ; 35, 482.

[11] J. Lindhard, *K. Dan. Vidensk. Selsk. Mat.-Fys. Medd.* **1954** ; 28(8), 1.

[12] J.M. Fernandez-Varea, F. Salvat, M. Dingfelder, D. Liljequist, *Nucl. Instrum. Meth. Phys. Res.* B **2005** ; 229, 187.

[13] K. Iakoubovskii, K. Mitsuishi, Y. Nakayama, K. Furuya, *Phys. Rev. B* **2008** ; 77, 104102.

[14] M.R. McCartney, M. Gajdardziska-Josifovska, *Ultramicroscopy*, **1994** ; 53 , 283.

[15] Y.-G. Wang, H.-R. Liu, Q.-B. Yang, Z. Zhang, *Chin. Phys. Lett.* **2003** ; 20 , 888.

[16] H. Shinotsuka, S. Tanuma, C. J. Powell, D. R. Penn, *Nucl. Instrum. Methods Phys. Res. B*, **2012** ; 270, 75.

[17] J.M. Fernandez-Varea, D. Liljequist, S. Csillag, R. Raty, F. Salvat, *Nucl. Instrum. Methods Phys. Res. B* **1996** ; 108 , 35.

Author Manuscript:
Published in final edited form as: *Surf. Interface Anal.* Volume 47, Issue 9, Pages 871-888, September 2015. https://doi.org/10.1002/sia.5789

[18] D. E. Cullen, J. H. Hubbell, L. Kissel, *EPDL97, The Evaluated Data Library, 1997 Version,* UCRL-50400, Vol. 6, Rev. 5 (Sep 19, 1997); http://ftp.esrf.eu/pub/scisoft/xop2.3/DabaxFiles/.

[19] S. Tanuma, C. J. Powell, D. R. Penn, *J. Electron Spectrosc. Relat. Phenom.* **1993** ; 62, 95.

[20] S. Tanuma, C. J. Powell, D. R. Penn, *Surf. Interface Anal.* **1993** ; 20, 77.

[21] S. Tanuma, C. J. Powell, D. R. Penn, *J. Electron Spectrosc. Relat. Phenom.* **1990** ; 52, 285

[22] H. Bethe, *Ann. Physik* **1930** ; 5, 325

[23] M. Inokuti, *Rev. Mod. Phys.* **1971** ; 43, 297.

[24] U. Fano, *Phys. Rev.* **1954** ; 95, 1198.

[25] S. Tanuma, C. J. Powell, D. R. Penn, *Surf. Interface Anal.* **2003** ; 35, 268.

[26] E. T. Arakawa, T. A. Callcott, and Y.-C. Chang, in *Handbook of Optical Constants of Solids II* (ed. E. D. Palik), Academic Press, New York, **1991**, p. 421.

[27] S. Tanuma, T. Shiratori, T. Kimura, K. Goto, S. Ichimura, C. J. Powell, *Surf. Interface Anal.* **2005** ; 37, 833.

[28] W. S. M. Werner, C. Tomastik, T. Cabela, G. Richter, H. Störi, *Surf. Sci.* **2000** ; 470, L123.

[29] W. S. M. Werner, C. Tomastik, T. Cabela, G. Richter, H. Störi, *J. Electron Spectrosc. Relat. Phenom.* **2001** ; 113, 127.

Author Manuscript:
Published in final edited form as: *Surf. Interface Anal.* Volume 47, Issue 9, Pages 871-888, September 2015. https://doi.org/10.1002/sia.5789

Table 1. List of elemental solids with values of Z, Z_{eff} from Eqn (18), and percentage errors in the f-sum rule.

Element	Z	Z_{eff} (1MeV)	Error in f-sum rule (%)
Li	3	3.06	2.1
Be	4	4.10	2.4
C (graphite)	6	6.29	4.8
C (diamond)	6	5.97	-0.5
C (glassy)	6	5.77	-3.9
Na	11	11.14	1.3
Mg	12	13.28	10.7
Al	13	13.13	1.0
Si	14	14.10	0.7
K	19	17.75	-6.6
Sc	21	22.94	9.3
Ti	22	21.95	-0.2
V	23	22.87	-0.6
Cr	24	22.38	-6.8
Fe	26	24.00	-7.7
Co	27	26.68	-1.2
Ni	28	27.48	-1.9
Cu	29	28.71	-1.0
Ge	32	32.89	2.8
Y	39	38.27	-1.9
Nb	41	38.52	-6.1
Mo	42	40.21	-4.3
Ru	44	42.23	-4.0
Rh	45	44.98	0.0
Pd	46	45.88	-0.3
Ag	47	51.00	8.5
In	49	48.43	-1.2
Sn	50	49.92	-0.2
Cs	55	50.73	-7.8
Gd	64	63.90	-0.2
Tb	65	66.55	2.4
Dy	66	68.12	3.2
Hf	72	71.46	-0.7
Ta	73	72.67	-0.4
W	74	73.46	-0.7
Re	75	74.22	-1.0
Os	76	73.61	-3.1
Ir	77	75.80	-1.6
Pt	78	77.19	-1.0
Au	79	78.38	-0.8
Bi	83	86.27	3.9

Author Manuscript:
Published in final edited form as: *Surf. Interface Anal*. Volume 47, Issue 9, Pages 871-888, September 2015. https://doi.org/10.1002/sia.5789

Table 2. Calculated IMFPs for the 41 elemental solids as a function of electron kinetic energy T with respect to the Fermi level E_f.

	Inelastic mean free path (nm)									
T(eV)	Li	Be	C (graphite)	C (diamond)	C (glassy)	Na	Mg	Al	Si	K
54.6	0.485	0.358	0.463	0.649	0.580	0.527	0.410	0.357	0.419	0.766
60.3	0.513	0.362	0.445	0.592	0.580	0.560	0.427	0.368	0.429	0.799
66.7	0.545	0.370	0.436	0.546	0.584	0.596	0.446	0.381	0.443	0.834
73.7	0.580	0.380	0.432	0.511	0.591	0.635	0.468	0.397	0.459	0.873
81.5	0.618	0.393	0.434	0.489	0.603	0.677	0.493	0.415	0.479	0.915
90.0	0.659	0.408	0.439	0.477	0.619	0.721	0.520	0.435	0.501	0.958
99.5	0.705	0.426	0.449	0.473	0.638	0.768	0.549	0.458	0.526	1.01
109.9	0.754	0.447	0.461	0.476	0.660	0.818	0.581	0.483	0.553	1.06
121.5	0.807	0.470	0.477	0.483	0.687	0.871	0.617	0.511	0.584	1.13
134.3	0.865	0.496	0.496	0.495	0.717	0.929	0.654	0.541	0.618	1.20
148.4	0.928	0.524	0.518	0.510	0.751	0.990	0.694	0.575	0.656	1.28
164.0	0.994	0.556	0.543	0.528	0.789	1.06	0.737	0.611	0.697	1.37
181.3	1.07	0.591	0.571	0.551	0.833	1.13	0.784	0.651	0.742	1.47
200.3	1.14	0.629	0.602	0.576	0.880	1.21	0.833	0.693	0.791	1.57
221.4	1.23	0.670	0.637	0.605	0.933	1.29	0.886	0.739	0.844	1.69
244.7	1.32	0.716	0.676	0.638	0.992	1.38	0.943	0.788	0.902	1.82
270.4	1.42	0.766	0.719	0.675	1.06	1.48	1.01	0.841	0.965	1.96
298.9	1.53	0.820	0.766	0.715	1.13	1.59	1.07	0.899	1.03	2.11
330.3	1.65	0.879	0.817	0.760	1.20	1.71	1.15	0.960	1.10	2.27
365.0	1.77	0.942	0.873	0.809	1.29	1.83	1.23	1.03	1.18	2.45
403.4	1.92	1.01	0.935	0.863	1.38	1.97	1.32	1.10	1.27	2.65
445.9	2.07	1.08	1.00	0.922	1.48	2.13	1.41	1.18	1.36	2.87
492.7	2.24	1.17	1.08	0.986	1.59	2.29	1.52	1.27	1.46	3.10
544.6	2.42	1.25	1.16	1.06	1.71	2.48	1.63	1.36	1.56	3.35
601.8	2.62	1.35	1.24	1.13	1.84	2.67	1.76	1.46	1.68	3.63
665.1	2.84	1.46	1.34	1.22	1.98	2.89	1.90	1.57	1.81	3.93
735.1	3.08	1.57	1.44	1.31	2.14	3.13	2.04	1.69	1.95	4.26
812.4	3.34	1.69	1.56	1.41	2.31	3.39	2.21	1.83	2.10	4.62
897.8	3.62	1.83	1.68	1.52	2.49	3.67	2.38	1.97	2.26	5.01
992.3	3.93	1.98	1.81	1.64	2.69	3.97	2.58	2.13	2.44	5.43
1096.6	4.27	2.14	1.96	1.76	2.91	4.31	2.79	2.30	2.64	5.89
1212.0	4.64	2.32	2.12	1.90	3.14	4.67	3.02	2.49	2.85	6.40

Author Manuscript:
Published in final edited form as: *Surf. Interface Anal*. Volume 47, Issue 9, Pages 871-888, September 2015. https://doi.org/10.1002/sia.5789

1339.4	5.04	2.51	2.29	2.06	3.40	5.07	3.27	2.69	3.08	6.94
1480.3	5.48	2.72	2.48	2.22	3.68	5.51	3.54	2.91	3.34	7.54
1636.0	5.96	2.95	2.68	2.40	3.98	5.98	3.84	3.15	3.62	8.18
1808.0	6.48	3.20	2.90	2.60	4.31	6.50	4.16	3.42	3.92	8.89
1998.2	7.05	3.47	3.15	2.81	4.67	7.06	4.52	3.71	4.25	9.66
2208.3	7.67	3.77	3.41	3.04	5.07	7.68	4.90	4.02	4.61	10.50
2440.6	8.35	4.09	3.70	3.30	5.50	8.35	5.32	4.36	5.00	11.42
2697.3	9.09	4.44	4.02	3.57	5.96	9.08	5.78	4.74	5.42	12.42
2981.0	9.90	4.83	4.36	3.87	6.47	9.88	6.28	5.14	5.89	13.51
3294.5	10.78	5.25	4.73	4.20	7.03	10.75	6.83	5.59	6.40	14.69
3641.0	11.74	5.70	5.14	4.56	7.64	11.70	7.42	6.07	6.95	15.99
4023.9	12.78	6.20	5.58	4.94	8.29	12.73	8.07	6.59	7.55	17.40
4447.1	13.92	6.74	6.06	5.37	9.01	13.86	8.77	7.17	8.21	18.94
4914.8	15.17	7.33	6.59	5.83	9.80	15.09	9.54	7.79	8.92	20.62
5431.7	16.53	7.97	7.16	6.33	10.65	16.43	10.37	8.47	9.70	22.45
6002.9	18.01	8.67	7.79	6.88	11.58	17.89	11.28	9.21	10.54	24.45
6634.2	19.62	9.43	8.47	7.47	12.59	19.48	12.27	10.02	11.47	26.62
7332.0	21.37	10.26	9.20	8.11	13.69	21.21	13.35	10.89	12.47	28.98
8103.1	23.29	11.17	10.01	8.82	14.89	23.09	14.53	11.85	13.56	31.56
8955.3	25.37	12.15	10.88	9.58	16.19	25.14	15.80	12.89	14.75	34.37
9897.1	27.63	13.21	11.83	10.41	17.61	27.37	17.19	14.02	16.04	37.42
10938.0	30.10	14.38	12.87	11.31	19.15	29.80	18.70	15.24	17.44	40.74
12088.4	32.78	15.64	13.99	12.29	20.82	32.44	20.34	16.58	18.97	44.35
13359.7	35.70	17.01	15.21	13.35	22.64	35.31	22.12	18.02	20.62	48.27
14764.8	38.87	18.50	16.53	14.50	24.61	38.42	24.06	19.59	22.42	52.53
16317.6	42.30	20.11	17.96	15.76	26.75	41.80	26.16	21.30	24.37	57.16
18033.7	46.03	21.86	19.52	17.11	29.06	45.47	28.43	23.14	26.48	62.17
19930.4	50.07	23.75	21.20	18.57	31.57	49.44	30.89	25.14	28.77	67.60
22026.5	54.45	25.80	23.02	20.16	34.29	53.74	33.56	27.31	31.25	73.49
24343.0	59.19	28.02	24.99	21.87	37.23	58.39	36.44	29.65	33.92	79.85
26903.2	64.30	30.41	27.11	23.72	40.40	63.41	39.55	32.17	36.81	86.72
29732.6	69.83	32.99	29.40	25.71	43.82	68.83	42.91	34.90	39.93	94.14
32859.6	75.78	35.77	31.87	27.86	47.50	74.68	46.53	37.83	43.28	102.1
36315.5	82.19	38.77	34.52	30.16	51.46	80.96	50.41	40.98	46.89	110.7
40134.8	89.07	41.98	37.37	32.64	55.71	87.71	54.59	44.37	50.77	120.0
44355.9	96.45	45.42	40.42	35.29	60.27	94.95	59.06	48.00	54.92	129.9

Author Manuscript:
Published in final edited form as: *Surf. Interface Anal*. Volume 47, Issue 9, Pages 871-888, September 2015. https://doi.org/10.1002/sia.5789

49020.8	104.4	49.10	43.69	38.13	65.14	102.7	63.85	51.89	59.36	140.5
54176.4	112.8	53.03	47.17	41.15	70.35	111.0	68.96	56.03	64.10	151.8
59874.1	121.8	57.22	50.88	44.37	75.89	119.8	74.41	60.45	69.15	163.9
66171.2	131.4	61.67	54.83	47.80	81.77	129.2	80.19	65.14	74.52	176.7
73130.4	141.5	66.38	59.00	51.42	88.01	139.1	86.32	70.11	80.20	190.3
80821.6	152.2	71.36	63.41	55.24	94.60	149.6	92.79	75.36	86.20	204.6
89321.7	163.5	76.61	68.05	59.27	101.5	160.6	99.61	80.88	92.52	219.7
98715.8	175.3	82.11	72.93	63.49	108.8	172.2	106.8	86.68	99.15	235.6
109097.8	187.7	87.86	78.02	67.91	116.4	184.4	114.2	92.74	106.1	252.2
120571.7	200.6	93.85	83.32	72.50	124.3	197.0	122.0	99.05	113.3	269.5
133252.4	214.0	100.1	88.81	77.26	132.5	210.1	130.1	105.6	120.8	287.4
147266.6	227.8	106.5	94.49	82.18	141.0	223.6	138.4	112.3	128.5	305.9
162754.8	242.1	113.1	100.3	87.22	149.7	237.5	147.0	119.3	136.4	325.0
179871.9	256.6	119.8	106.3	92.38	158.6	251.7	155.7	126.4	144.5	344.4
198789.2	271.3	126.6	112.3	97.61	167.7	266.2	164.6	133.6	152.8	364.2

Author Manuscript:
Published in final edited form as: *Surf. Interface Anal*. Volume 47, Issue 9, Pages 871-888, September 2015. https://doi.org/10.1002/sia.5789

Table 2 (continued)

	Inelastic mean free path (nm)									
T (eV)	Sc	Ti	V	Cr	Fe	Co	Ni	Cu	Ge	Y
54.6	0.487	0.427	0.463	0.447	0.432	0.493	0.486	0.502	0.408	0.543
60.3	0.486	0.426	0.461	0.438	0.430	0.480	0.479	0.497	0.419	0.544
66.7	0.487	0.429	0.463	0.434	0.433	0.471	0.475	0.495	0.432	0.547
73.7	0.490	0.435	0.468	0.434	0.438	0.466	0.472	0.496	0.447	0.551
81.5	0.495	0.443	0.476	0.438	0.447	0.465	0.473	0.500	0.465	0.554
90.0	0.502	0.452	0.486	0.445	0.458	0.468	0.476	0.507	0.484	0.559
99.5	0.509	0.461	0.498	0.456	0.471	0.474	0.482	0.516	0.506	0.567
109.9	0.516	0.468	0.509	0.469	0.486	0.483	0.490	0.528	0.530	0.580
121.5	0.527	0.477	0.522	0.484	0.503	0.494	0.501	0.542	0.557	0.599
134.3	0.544	0.489	0.535	0.499	0.523	0.507	0.514	0.559	0.587	0.623
148.4	0.565	0.507	0.550	0.516	0.544	0.521	0.529	0.578	0.618	0.653
164.0	0.592	0.529	0.567	0.536	0.564	0.534	0.547	0.599	0.653	0.687
181.3	0.623	0.555	0.589	0.558	0.588	0.550	0.567	0.623	0.691	0.727
200.3	0.658	0.584	0.614	0.583	0.614	0.568	0.588	0.650	0.731	0.770
221.4	0.697	0.617	0.643	0.612	0.643	0.591	0.612	0.679	0.775	0.819
244.7	0.740	0.654	0.675	0.644	0.676	0.616	0.638	0.711	0.823	0.873
270.4	0.788	0.695	0.712	0.680	0.713	0.645	0.668	0.746	0.875	0.932
298.9	0.840	0.740	0.753	0.720	0.753	0.678	0.701	0.785	0.931	1.00
330.3	0.898	0.789	0.798	0.764	0.797	0.714	0.738	0.828	0.991	1.07
365.0	0.961	0.843	0.848	0.812	0.845	0.755	0.779	0.875	1.06	1.15
403.4	1.03	0.902	0.903	0.865	0.898	0.799	0.824	0.927	1.13	1.23
445.9	1.11	0.966	0.964	0.923	0.957	0.850	0.876	0.983	1.21	1.32
492.7	1.19	1.04	1.03	0.986	1.02	0.903	0.930	1.04	1.29	1.42
544.6	1.28	1.11	1.10	1.06	1.09	0.962	0.990	1.11	1.38	1.53
601.8	1.38	1.20	1.18	1.13	1.17	1.03	1.06	1.19	1.48	1.65
665.1	1.48	1.29	1.27	1.21	1.25	1.10	1.13	1.27	1.59	1.78
735.1	1.60	1.39	1.37	1.31	1.34	1.18	1.21	1.35	1.71	1.91
812.4	1.72	1.50	1.47	1.40	1.44	1.26	1.30	1.45	1.83	2.06
897.8	1.86	1.62	1.58	1.51	1.55	1.36	1.39	1.56	1.97	2.23
992.3	2.01	1.75	1.71	1.63	1.67	1.46	1.49	1.67	2.12	2.40
1096.6	2.18	1.89	1.84	1.76	1.80	1.57	1.61	1.80	2.29	2.59
1212.0	2.35	2.04	1.99	1.90	1.94	1.69	1.73	1.93	2.47	2.80
1339.4	2.55	2.20	2.15	2.05	2.09	1.82	1.86	2.08	2.67	3.03

Author Manuscript:
Published in final edited form as: *Surf. Interface Anal*. Volume 47, Issue 9, Pages 871-888, September 2015. https://doi.org/10.1002/sia.5789

1480.3	2.76	2.39	2.32	2.21	2.26	1.96	2.01	2.25	2.88	3.28
1636.0	2.99	2.58	2.51	2.39	2.44	2.12	2.17	2.42	3.11	3.54
1808.0	3.24	2.80	2.72	2.59	2.64	2.29	2.35	2.62	3.37	3.84
1998.2	3.51	3.03	2.94	2.80	2.85	2.48	2.53	2.83	3.65	4.15
2208.3	3.80	3.29	3.18	3.04	3.09	2.68	2.74	3.06	3.95	4.50
2440.6	4.13	3.56	3.45	3.29	3.34	2.90	2.97	3.31	4.28	4.88
2697.3	4.48	3.86	3.73	3.56	3.62	3.14	3.21	3.58	4.64	5.29
2981.0	4.86	4.19	4.05	3.86	3.92	3.40	3.48	3.88	5.03	5.74
3294.5	5.27	4.55	4.39	4.18	4.25	3.68	3.77	4.20	5.46	6.23
3641.0	5.73	4.94	4.76	4.54	4.61	3.99	4.08	4.55	5.92	6.76
4023.9	6.22	5.36	5.16	4.92	5.00	4.33	4.43	4.93	6.43	7.34
4447.1	6.76	5.82	5.60	5.34	5.42	4.69	4.80	5.35	6.98	7.97
4914.8	7.34	6.32	6.08	5.79	5.89	5.09	5.20	5.80	7.58	8.66
5431.7	7.98	6.87	6.60	6.29	6.39	5.52	5.64	6.29	8.23	9.41
6002.9	8.67	7.46	7.16	6.83	6.93	5.99	6.13	6.83	8.94	10.22
6634.2	9.43	8.11	7.78	7.42	7.53	6.50	6.65	7.41	9.71	11.11
7332.0	10.25	8.81	8.45	8.06	8.17	7.06	7.21	8.04	10.55	12.08
8103.1	11.14	9.58	9.18	8.75	8.88	7.66	7.83	8.72	11.46	13.13
8955.3	12.11	10.41	9.97	9.51	9.64	8.32	8.50	9.47	12.46	14.27
9897.1	13.17	11.32	10.83	10.33	10.47	9.03	9.23	10.28	13.54	15.51
10938.0	14.32	12.30	11.77	11.22	11.37	9.80	10.02	11.16	14.71	16.86
12088.4	15.57	13.37	12.79	12.19	12.35	10.64	10.88	12.12	15.99	18.33
13359.7	16.92	14.53	13.89	13.24	13.41	11.56	11.81	13.15	17.37	19.92
14764.8	18.39	15.79	15.09	14.38	14.57	12.55	12.82	14.28	18.87	21.64
16317.6	19.98	17.15	16.39	15.61	15.82	13.62	13.92	15.50	20.50	23.51
18033.7	21.71	18.63	17.79	16.95	17.17	14.78	15.10	16.82	22.26	25.54
19930.4	23.58	20.23	19.31	18.40	18.64	16.04	16.39	18.25	24.17	27.74
22026.5	25.60	21.96	20.96	19.97	20.22	17.39	17.77	19.79	26.23	30.11
24343.0	27.79	23.84	22.74	21.66	21.93	18.86	19.27	21.46	28.46	32.68
26903.2	30.15	25.86	24.65	23.49	23.78	20.45	20.89	23.26	30.87	35.45
29732.6	32.70	28.03	26.72	25.46	25.77	22.15	22.63	25.20	33.47	38.43
32859.6	35.44	30.38	28.95	27.58	27.91	23.99	24.51	27.29	36.27	41.65
36315.5	38.38	32.90	31.34	29.86	30.22	25.96	26.53	29.53	39.27	45.11
40134.8	41.54	35.61	33.91	32.30	32.69	28.08	28.69	31.94	42.50	48.82
44355.9	44.93	38.51	36.66	34.93	35.34	30.35	31.01	34.52	45.96	52.79
49020.8	48.56	41.61	39.60	37.73	38.17	32.78	33.48	37.27	49.65	57.05

Author Manuscript:
Published in final edited form as: *Surf. Interface Anal*. Volume 47, Issue 9, Pages 871-888, September 2015. https://doi.org/10.1002/sia.5789

54176.4	52.43	44.92	42.74	40.72	41.19	35.36	36.12	40.21	53.60	61.59
59874.1	56.55	48.44	46.08	43.90	44.41	38.12	38.94	43.34	57.80	66.42
66171.2	60.92	52.18	49.63	47.28	47.82	41.04	41.92	46.66	62.26	71.55
73130.4	65.56	56.15	53.39	50.86	51.43	44.13	45.08	50.18	66.98	76.99
80821.6	70.45	60.33	57.35	54.63	55.25	47.40	48.42	53.89	71.97	82.73
89321.7	75.60	64.74	61.53	58.61	59.27	50.84	51.93	57.80	77.23	88.78
98715.8	81.01	69.36	65.91	62.78	63.48	54.45	55.61	61.90	82.73	95.12
109097.8	86.66	74.19	70.48	67.14	67.88	58.21	59.46	66.18	88.49	101.7
120571.7	92.54	79.22	75.24	71.68	72.47	62.13	63.46	70.63	94.49	108.6
133252.4	98.64	84.43	80.18	76.38	77.22	66.20	67.61	75.25	100.7	115.8
147266.6	104.9	89.81	85.27	81.23	82.12	70.39	71.89	80.01	107.1	123.2
162754.8	111.4	95.34	90.50	86.21	87.15	74.69	76.28	84.90	113.7	130.8
179871.9	118.0	101.0	95.85	91.30	92.29	79.09	80.77	89.90	120.4	138.5
198789.2	124.7	106.7	101.3	96.47	97.51	83.55	85.33	94.97	127.3	146.4

Author Manuscript:
Published in final edited form as: *Surf. Interface Anal*. Volume 47, Issue 9, Pages 871-888, September 2015. https://doi.org/10.1002/sia.5789

Table 2 (continued)

	Inelastic mean free path (nm)									
T(eV)	Nb	Mo	Ru	Rh	Pd	Ag	In	Sn	Cs	Gd
54.6	0.587	0.509	0.501	0.482	0.490	0.609	0.482	0.581	0.666	0.436
60.3	0.576	0.488	0.482	0.466	0.475	0.591	0.494	0.590	0.699	0.436
66.7	0.571	0.476	0.464	0.452	0.462	0.575	0.507	0.601	0.737	0.438
73.7	0.569	0.469	0.449	0.441	0.452	0.562	0.521	0.616	0.778	0.442
81.5	0.570	0.467	0.440	0.431	0.443	0.550	0.537	0.633	0.825	0.449
90.0	0.572	0.468	0.435	0.426	0.438	0.541	0.553	0.652	0.876	0.460
99.5	0.573	0.470	0.434	0.424	0.436	0.534	0.571	0.672	0.934	0.474
109.9	0.573	0.473	0.436	0.426	0.437	0.531	0.590	0.695	1.00	0.491
121.5	0.574	0.477	0.440	0.431	0.440	0.530	0.610	0.718	1.07	0.511
134.3	0.578	0.482	0.447	0.438	0.446	0.531	0.632	0.743	1.14	0.534
148.4	0.588	0.491	0.456	0.446	0.454	0.536	0.655	0.769	1.22	0.560
164.0	0.605	0.505	0.466	0.456	0.464	0.543	0.680	0.796	1.31	0.589
181.3	0.627	0.523	0.479	0.468	0.476	0.552	0.708	0.825	1.41	0.622
200.3	0.655	0.545	0.495	0.482	0.491	0.565	0.739	0.856	1.51	0.657
221.4	0.688	0.572	0.515	0.500	0.509	0.581	0.773	0.891	1.63	0.697
244.7	0.725	0.603	0.540	0.522	0.532	0.600	0.811	0.930	1.75	0.741
270.4	0.768	0.638	0.569	0.548	0.558	0.625	0.852	0.973	1.88	0.788
298.9	0.815	0.677	0.601	0.578	0.589	0.654	0.898	1.02	2.01	0.840
330.3	0.868	0.720	0.638	0.612	0.625	0.688	0.951	1.08	2.16	0.896
365.0	0.925	0.768	0.678	0.650	0.664	0.727	1.01	1.14	2.32	0.958
403.4	0.989	0.820	0.723	0.692	0.707	0.771	1.08	1.21	2.49	1.02
445.9	1.06	0.877	0.772	0.739	0.755	0.821	1.15	1.29	2.69	1.10
492.7	1.13	0.939	0.826	0.789	0.807	0.875	1.23	1.38	2.90	1.17
544.6	1.22	1.01	0.884	0.845	0.864	0.934	1.32	1.47	3.13	1.26
601.8	1.30	1.08	0.948	0.906	0.926	0.999	1.42	1.58	3.38	1.35
665.1	1.40	1.16	1.02	0.972	0.994	1.07	1.52	1.70	3.66	1.45
735.1	1.51	1.25	1.09	1.04	1.07	1.15	1.64	1.82	3.96	1.56
812.4	1.62	1.34	1.18	1.12	1.15	1.23	1.76	1.96	4.29	1.68
897.8	1.75	1.45	1.27	1.21	1.24	1.32	1.90	2.11	4.65	1.81
992.3	1.88	1.56	1.36	1.30	1.33	1.42	2.05	2.27	5.04	1.95
1096.6	2.02	1.68	1.47	1.40	1.44	1.53	2.21	2.45	5.47	2.10
1212.0	2.18	1.81	1.58	1.51	1.55	1.65	2.39	2.64	5.93	2.27
1339.4	2.35	1.95	1.71	1.63	1.67	1.78	2.58	2.85	6.44	2.46

Author Manuscript:
Published in final edited form as: *Surf. Interface Anal*. Volume 47, Issue 9, Pages 871-888, September 2015. https://doi.org/10.1002/sia.5789

1480.3	2.54	2.11	1.84	1.76	1.81	1.92	2.79	3.08	6.99	2.66
1636.0	2.74	2.27	1.99	1.90	1.95	2.07	3.02	3.33	7.59	2.87
1808.0	2.96	2.46	2.15	2.05	2.11	2.23	3.26	3.60	8.25	3.11
1998.2	3.20	2.65	2.32	2.22	2.28	2.41	3.53	3.90	8.96	3.37
2208.3	3.46	2.87	2.51	2.40	2.46	2.60	3.82	4.22	9.74	3.65
2440.6	3.75	3.10	2.71	2.59	2.66	2.81	4.14	4.56	10.59	3.95
2697.3	4.05	3.36	2.94	2.80	2.88	3.04	4.48	4.94	11.52	4.29
2981.0	4.39	3.64	3.18	3.03	3.12	3.29	4.86	5.35	12.53	4.65
3294.5	4.76	3.94	3.44	3.28	3.38	3.56	5.27	5.80	13.63	5.04
3640.9	5.16	4.27	3.73	3.56	3.66	3.86	5.71	6.28	14.83	5.47
4023.9	5.59	4.63	4.04	3.86	3.97	4.18	6.19	6.81	16.13	5.94
4447.1	6.06	5.02	4.38	4.18	4.30	4.53	6.72	7.39	17.55	6.45
4914.8	6.58	5.45	4.75	4.53	4.66	4.91	7.29	8.01	19.10	7.00
5431.7	7.14	5.91	5.16	4.92	5.06	5.32	7.92	8.69	20.78	7.61
6002.9	7.75	6.41	5.59	5.34	5.49	5.77	8.59	9.43	22.62	8.26
6634.2	8.41	6.96	6.07	5.79	5.96	6.26	9.33	10.24	24.62	8.97
7332.0	9.13	7.56	6.59	6.28	6.47	6.80	10.13	11.12	26.80	9.75
8103.1	9.92	8.21	7.15	6.82	7.02	7.37	11.01	12.07	29.17	10.59
8955.3	10.77	8.91	7.77	7.41	7.62	8.00	11.96	13.11	31.76	11.51
9897.1	11.69	9.68	8.43	8.04	8.28	8.69	12.99	14.23	34.57	12.50
10938.0	12.70	10.51	9.16	8.73	8.99	9.43	14.11	15.46	37.62	13.58
12088.4	13.79	11.42	9.94	9.48	9.76	10.24	15.33	16.79	40.95	14.76
13359.7	14.98	12.39	10.79	10.29	10.59	11.11	16.65	18.23	44.56	16.03
14764.8	16.26	13.46	11.72	11.17	11.50	12.06	18.08	19.79	48.48	17.41
16317.6	17.66	14.61	12.72	12.13	12.48	13.09	19.63	21.49	52.73	18.91
18033.7	19.16	15.86	13.80	13.16	13.55	14.20	21.32	23.32	57.34	20.54
19930.4	20.79	17.21	14.98	14.28	14.70	15.41	23.14	25.31	62.34	22.29
22026.5	22.56	18.67	16.25	15.49	15.95	16.71	25.11	27.46	67.76	24.20
24343.0	24.46	20.25	17.62	16.80	17.29	18.12	27.24	29.78	73.61	26.25
26903.2	26.52	21.95	19.10	18.21	18.74	19.63	29.53	32.28	79.93	28.47
29732.6	28.74	23.78	20.69	19.72	20.31	21.27	32.01	34.98	86.75	30.86
32859.6	31.12	25.75	22.40	21.36	21.99	23.03	34.67	37.89	94.10	33.43
36315.5	33.69	27.88	24.25	23.11	23.80	24.92	37.53	41.01	102.0	36.20
40134.8	36.44	30.15	26.22	25.00	25.74	26.94	40.61	44.36	110.5	39.17
44355.9	39.39	32.59	28.34	27.02	27.82	29.11	43.90	47.94	119.6	42.35
49020.8	42.54	35.20	30.61	29.18	30.04	31.43	47.42	51.78	129.3	45.75

Author Manuscript:
Published in final edited form as: *Surf. Interface Anal*. Volume 47, Issue 9, Pages 871-888, September 2015. https://doi.org/10.1002/sia.5789

54176.4	45.90	37.98	33.02	31.48	32.41	33.91	51.18	55.87	139.8	49.38
59874.1	49.48	40.94	35.59	33.93	34.94	36.54	55.18	60.23	150.8	53.25
66171.2	53.28	44.08	38.32	36.53	37.62	39.34	59.42	64.85	162.6	57.35
73130.4	57.30	47.41	41.21	39.28	40.45	42.30	63.92	69.75	175.1	61.70
80821.6	61.55	50.92	44.26	42.19	43.45	45.43	68.67	74.92	188.3	66.29
89321.7	66.02	54.62	47.47	45.25	46.60	48.72	73.66	80.36	202.2	71.12
98715.8	70.71	58.50	50.84	48.46	49.91	52.16	78.90	86.07	216.8	76.19
109097.8	75.61	62.55	54.36	51.81	53.36	55.77	84.38	92.03	232.0	81.49
120571.7	80.70	66.77	58.02	55.30	56.95	59.52	90.08	98.24	247.9	87.00
133252.4	85.99	71.14	61.81	58.91	60.68	63.40	95.99	104.7	264.4	92.71
147266.6	91.44	75.65	65.72	62.64	64.52	67.41	102.1	111.3	281.4	98.61
162754.8	97.03	80.27	69.74	66.47	68.47	71.52	108.3	118.1	298.8	104.7
179871.9	102.8	85.00	73.85	70.38	72.49	75.72	114.7	125.1	316.7	110.8
198789.2	108.6	89.81	78.02	74.35	76.59	79.99	121.2	132.1	334.8	117.1

Author Manuscript:
Published in final edited form as: *Surf. Interface Anal*. Volume 47, Issue 9, Pages 871-888, September 2015. https://doi.org/10.1002/sia.5789

Table 2. (continued)

	Inelastic mean free path (nm)										
T (eV)	Tb	Dy	Hf	Ta	W	Re	Os	Ir	Pt	Au	Bi
54.6	0.436	0.475	0.562	0.483	0.521	0.531	0.551	0.523	0.501	0.516	0.496
60.3	0.434	0.471	0.560	0.474	0.495	0.497	0.526	0.501	0.483	0.502	0.504
66.7	0.435	0.469	0.561	0.470	0.477	0.470	0.503	0.480	0.467	0.491	0.515
73.7	0.436	0.470	0.563	0.469	0.466	0.452	0.484	0.461	0.453	0.480	0.528
81.5	0.438	0.472	0.566	0.470	0.461	0.442	0.471	0.448	0.442	0.471	0.542
90.0	0.440	0.474	0.570	0.473	0.461	0.438	0.465	0.440	0.436	0.465	0.558
99.5	0.445	0.479	0.575	0.478	0.465	0.438	0.464	0.436	0.435	0.461	0.575
109.9	0.453	0.487	0.581	0.484	0.471	0.440	0.467	0.437	0.437	0.460	0.593
121.5	0.465	0.499	0.590	0.491	0.478	0.445	0.472	0.442	0.442	0.462	0.613
134.3	0.481	0.514	0.601	0.500	0.485	0.451	0.479	0.448	0.450	0.468	0.634
148.4	0.500	0.533	0.616	0.511	0.494	0.460	0.487	0.457	0.460	0.476	0.656
164.0	0.523	0.556	0.635	0.525	0.506	0.470	0.496	0.468	0.472	0.487	0.680
181.3	0.550	0.583	0.659	0.543	0.521	0.483	0.509	0.481	0.488	0.501	0.707
200.3	0.579	0.613	0.687	0.564	0.540	0.499	0.526	0.497	0.506	0.519	0.736
221.4	0.612	0.646	0.719	0.589	0.562	0.519	0.546	0.516	0.527	0.539	0.769
244.7	0.648	0.683	0.755	0.617	0.588	0.542	0.569	0.539	0.550	0.563	0.807
270.4	0.688	0.724	0.796	0.649	0.617	0.569	0.596	0.565	0.577	0.591	0.849
298.9	0.732	0.769	0.840	0.685	0.650	0.599	0.627	0.595	0.608	0.621	0.896
330.3	0.780	0.818	0.889	0.724	0.686	0.632	0.662	0.628	0.642	0.656	0.949
365.0	0.833	0.872	0.943	0.767	0.726	0.669	0.700	0.665	0.680	0.695	1.01
403.4	0.890	0.930	1.00	0.815	0.770	0.710	0.741	0.706	0.722	0.737	1.07
445.9	0.953	0.995	1.07	0.866	0.818	0.754	0.787	0.750	0.768	0.785	1.14
492.7	1.02	1.06	1.14	0.923	0.871	0.802	0.837	0.799	0.818	0.836	1.22
544.6	1.09	1.14	1.21	0.984	0.928	0.855	0.892	0.851	0.872	0.893	1.31
601.8	1.17	1.22	1.29	1.05	0.990	0.912	0.951	0.909	0.931	0.954	1.40
665.1	1.26	1.31	1.38	1.12	1.06	0.974	1.02	0.971	0.996	1.02	1.51
735.1	1.35	1.41	1.48	1.20	1.13	1.04	1.09	1.04	1.07	1.09	1.62
812.4	1.46	1.51	1.59	1.29	1.21	1.12	1.16	1.11	1.14	1.17	1.74
897.8	1.57	1.63	1.70	1.38	1.30	1.20	1.24	1.19	1.22	1.26	1.87
992.3	1.69	1.75	1.83	1.48	1.39	1.28	1.33	1.28	1.31	1.35	2.02
1096.6	1.83	1.89	1.97	1.59	1.49	1.38	1.43	1.37	1.41	1.45	2.17
1212.0	1.97	2.04	2.12	1.71	1.61	1.48	1.54	1.47	1.52	1.56	2.34
1339.4	2.13	2.20	2.28	1.84	1.73	1.59	1.65	1.59	1.63	1.68	2.53

Author Manuscript:
Published in final edited form as: *Surf. Interface Anal*. Volume 47, Issue 9, Pages 871-888, September 2015. https://doi.org/10.1002/sia.5789

1480.3	2.30	2.38	2.46	1.99	1.86	1.71	1.78	1.71	1.76	1.81	2.73
1636.0	2.49	2.57	2.65	2.14	2.00	1.85	1.91	1.84	1.89	1.96	2.95
1808.0	2.69	2.78	2.86	2.31	2.16	1.99	2.06	1.98	2.04	2.11	3.19
1998.2	2.92	3.00	3.08	2.49	2.33	2.15	2.22	2.14	2.20	2.28	3.44
2208.3	3.16	3.25	3.33	2.69	2.51	2.32	2.40	2.30	2.37	2.46	3.72
2440.6	3.42	3.52	3.60	2.91	2.71	2.50	2.59	2.49	2.56	2.66	4.03
2697.3	3.71	3.82	3.90	3.15	2.93	2.70	2.80	2.69	2.77	2.87	4.36
2981.0	4.02	4.14	4.22	3.40	3.17	2.92	3.02	2.90	3.00	3.10	4.72
3294.5	4.36	4.49	4.56	3.68	3.43	3.16	3.27	3.14	3.24	3.36	5.12
3640.9	4.74	4.87	4.94	3.99	3.71	3.42	3.53	3.40	3.51	3.64	5.54
4023.9	5.14	5.28	5.35	4.32	4.02	3.70	3.83	3.68	3.80	3.94	6.01
4447.1	5.58	5.73	5.80	4.68	4.35	4.01	4.14	3.98	4.11	4.27	6.52
4914.8	6.06	6.22	6.29	5.07	4.72	4.35	4.49	4.32	4.45	4.62	7.07
5431.7	6.58	6.75	6.82	5.50	5.11	4.71	4.86	4.68	4.83	5.01	7.67
6002.9	7.14	7.33	7.40	5.97	5.54	5.11	5.27	5.07	5.23	5.43	8.32
6634.2	7.76	7.96	8.03	6.47	6.01	5.54	5.71	5.50	5.68	5.89	9.04
7332.0	8.43	8.65	8.71	7.02	6.52	6.00	6.19	5.96	6.15	6.39	9.81
8103.1	9.16	9.39	9.45	7.62	7.07	6.51	6.72	6.46	6.68	6.94	10.65
8955.3	9.95	10.20	10.26	8.27	7.67	7.07	7.29	7.01	7.24	7.53	11.57
9897.1	10.81	11.08	11.13	8.97	8.32	7.67	7.90	7.61	7.86	8.17	12.56
10938.0	11.74	12.03	12.08	9.74	9.03	8.32	8.57	8.25	8.53	8.86	13.64
12088.4	12.76	13.07	13.12	10.57	9.80	9.03	9.30	8.95	9.25	9.62	14.81
13359.7	13.86	14.20	14.23	11.47	10.63	9.79	10.09	9.71	10.04	10.44	16.09
14764.8	15.06	15.42	15.45	12.44	11.53	10.62	10.94	10.54	10.89	11.32	17.47
16317.6	16.35	16.74	16.76	13.50	12.51	11.52	11.87	11.43	11.81	12.28	18.96
18033.7	17.75	18.17	18.18	14.64	13.56	12.50	12.87	12.39	12.81	13.33	20.58
19930.4	19.27	19.73	19.72	15.88	14.71	13.55	13.95	13.44	13.89	14.45	22.33
22026.5	20.92	21.40	21.38	17.22	15.95	14.69	15.13	14.57	15.06	15.67	24.23
24343.0	22.69	23.22	23.18	18.66	17.28	15.92	16.39	15.79	16.32	16.98	26.28
26903.2	24.61	25.17	25.12	20.22	18.72	17.25	17.75	17.10	17.68	18.40	28.48
29732.6	26.67	27.28	27.21	21.90	20.27	18.68	19.22	18.52	19.15	19.93	30.86
32859.6	28.90	29.55	29.46	23.71	21.94	20.21	20.80	20.04	20.72	21.57	33.43
36315.5	31.29	31.99	31.87	25.65	23.74	21.87	22.50	21.68	22.42	23.34	36.18
40134.8	33.85	34.61	34.47	27.74	25.66	23.64	24.33	23.44	24.24	25.23	39.14
44355.9	36.60	37.41	37.24	29.97	27.73	25.54	26.28	25.32	26.18	27.26	42.30
49020.8	39.54	40.41	40.21	32.36	29.93	27.57	28.36	27.33	28.26	29.43	45.69

Author Manuscript:
Published in final edited form as: *Surf. Interface Anal*. Volume 47, Issue 9, Pages 871-888, September 2015. https://doi.org/10.1002/sia.5789

54176.4	42.67	43.61	43.38	34.90	32.28	29.73	30.59	29.47	30.48	31.74	49.30
59874.1	46.01	47.02	46.74	37.61	34.78	32.03	32.95	31.75	32.85	34.20	53.14
66171.2	49.56	50.64	50.32	40.49	37.44	34.48	35.47	34.18	35.35	36.82	57.22
73130.4	53.31	54.47	54.11	43.53	40.24	37.07	38.12	36.74	38.01	39.58	61.55
80821.6	57.27	58.51	58.10	46.74	43.21	39.80	40.93	39.45	40.81	42.50	66.11
89321.7	61.44	62.76	62.31	50.12	46.33	42.67	43.88	42.29	43.75	45.57	70.91
98715.8	65.82	67.23	66.72	53.67	49.60	45.68	46.98	45.28	46.84	48.79	75.95
109097.8	70.39	71.89	71.32	57.37	53.02	48.83	50.21	48.39	50.07	52.16	81.21
120571.7	75.15	76.75	76.12	61.22	56.58	52.11	53.58	51.64	53.43	55.66	86.69
133252.4	80.08	81.78	81.08	65.21	60.26	55.50	57.06	55.00	56.91	59.29	92.36
147266.6	85.17	86.97	86.21	69.33	64.06	59.00	60.66	58.47	60.50	63.03	98.22
162754.8	90.40	92.30	91.47	73.56	67.96	62.59	64.35	62.03	64.18	66.87	104.2
179871.9	95.74	97.74	96.84	77.88	71.95	66.26	68.11	65.66	67.95	70.79	110.4
198789.2	101.2	103.3	102.3	82.26	75.99	69.99	71.94	69.35	71.77	74.78	116.6

Author Manuscript:
Published in final edited form as: *Surf. Interface Anal*. Volume 47, Issue 9, Pages 871-888, September 2015. https://doi.org/10.1002/sia.5789

Table 3. Values of the parameters β_r, γ_r, C_r and D_r found in the fits of Eqn (26) to the calculated IMFPs for each elemental solid and values of *RMS* calculated from Eqn (28).

	β_r(eV^{-1}nm^{-1})	γ_r (eV^{-1})	C_r (nm^{-1})	D_r (eV nm^{-1})	*RMS(%)*
Li	0.6520	0.4433	39.41	1273.0	0.31
Be	0.2884	0.1698	16.89	357.2	0.47
C	0.1816	0.1371	14.56	273.0	0.25
C	0.1376	0.1035	13.28	270.0	0.34
C (glassy)	0.1512	0.1461	11.93	282.1	0.26
Na	1.2545	0.3086	98.46	3761.2	0.37
Mg	0.6379	0.1661	44.01	1637.0	0.73
Al	0.3853	0.1291	18.23	617.0	0.82
Si	0.3063	0.1236	12.47	371.0	0.81
K	1.7481	0.3173	66.80	275.9	0.29
Sc	0.6005	0.1619	62.26	1496.0	0.62
Ti	0.3775	0.1394	40.35	1139.3	0.52
V	0.2610	0.0962	27.92	959.7	0.69
Cr	0.2021	0.0869	16.95	532.7	0.65
Fe	0.1496	0.0723	11.13	412.6	1.01
Co	0.1474	0.0621	13.06	481.2	1.26
Ni	0.1304	0.0584	10.70	408.6	1.23
Cu	0.1159	0.0537	7.55	300.7	1.24
Ge	0.4355	0.0823	19.43	785.2	0.94
Y	0.6971	0.1250	42.06	645.7	0.78
Nb	0.3168	0.0914	33.85	1055.8	1.00
Mo	0.2772	0.0852	26.50	779.8	0.81
Ru	0.2108	0.0787	21.60	663.8	0.60
Rh	0.2008	0.0770	21.72	705.8	0.64
Pd	0.1855	0.0833	21.59	700.4	0.67
Ag	0.1933	0.0652	23.46	861.5	1.07
In	0.6875	0.0925	68.48	2612.3	0.80
Sn	0.5018	0.0750	47.64	1925.2	1.22
Cs	3.0444	0.2464	108.45	3424.3	0.54
Gd	0.2892	0.0923	13.92	322.9	0.40
Tb	0.3334	0.1007	26.11	686.9	0.38
Dy	0.3189	0.0876	24.58	702.1	0.32
Hf	0.5541	0.0554	39.14	1495.3	0.48
Ta	0.4510	0.0515	30.45	1176.7	0.64
W	0.3599	0.0463	21.95	816.5	0.90
Re	0.3108	0.0469	19.98	697.5	0.79
Os	0.2535	0.0435	15.92	595.9	0.77
Ir	0.2334	0.0469	15.64	556.7	0.57
Pt	0.2163	0.0492	14.35	506.8	0.52
Au	0.2071	0.0577	18.53	660.7	0.47
Bi	0.5934	0.0768	51.83	2035.6	0.82

Author Manuscript:
Published in final edited form as: *Surf. Interface Anal.* Volume 47, Issue 9, Pages 871-888, September 2015. https://doi.org/10.1002/sia.5789

Table 4. Root-mean-square (RMS) percentage deviations between IMFPs from two forms of the relativistic TPP-2M equation, Eqns (25) and (29) and Eqns (26) and (29), and IMFPs calculated from optical data for the indicated elemental solids and for energies between 50 eV and 200 keV.

Element	*RMS* with Eqns (26) and (29) (%)	*RMS* with Eqns (25) and (29) (%)
Li	15.4	15.5
Be	22.5	22.4
C (graphite)	46.6	46.4
C (diamond)	70.7	70.4
C (glassy)	1.8	2.0
Na	3.9	3.8
Mg	8.5	8.3
Al	10.3	10.2
Si	3.7	3.9
K	2.9	3.0
Sc	24.2	24.0
Ti	19.3	19.1
V	7.2	7.1
Cr	4.1	4.0
Fe	3.8	4.0
Co	6.7	6.6
Ni	7.4	7.3
Cu	12.2	12.3
Ge	4.6	4.5
Y	13.2	13.1
Nb	4.9	5.0
Mo	5.2	5.1
Ru	3.8	3.7
Rh	5.6	5.5
Pd	4.6	4.6
Ag	9.0	9.0
In	19.4	19.3
Sn	5.6	5.6
Cs	34.7	34.5
Gd	6.9	7.1
Tb	8.9	8.8
Dy	3.1	3.0
Hf	11.8	11.6
Ta	15.0	14.9
W	7.0	6.9
Re	4.4	4.3
Os	8.2	8.3

Author Manuscript:
Published in final edited form as: *Surf. Interface Anal*. Volume 47, Issue 9, Pages 871-888, September 2015. https://doi.org/10.1002/sia.5789

Ir	8.3	8.5
Pt	10.7	10.9
Au	11.3	11.4
Bi	12.5	12.3

Author Manuscript:
Published in final edited form as: *Surf. Interface Anal.* Volume 47, Issue 9, Pages 871-888, September 2015. https://doi.org/10.1002/sia.5789

Figure Captions

Fig. 11. Plots of the differences between λ_{new} and λ_{old} as a function of electron energy for Cs, Gd, Tb, Dy, Hf, Ta, W, Re, Os, Ir, Pt, Au, and Bi. See caption to Fig. 9.

Fig. 12. Plots of the average absolute differences [$= \sum \left| \lambda_{new} - \lambda_{old} \right| / n$] and of the percentage root-mean-square deviations [$= 100 \sum \{ (\lambda_{new} - \lambda_{old}) / \lambda_{old} \} / n$] as a function of electron energy for the 41 elemental solids.

Fig. 13. Fano plots for Al, Cu, and Au based on Eqn (26). The solid and open circles represent IMFPs calculated with the relativistic FPA. The solid and dashed lines show curve-fit results with Eqns (26) and (25), respectively, for energies between 50 eV and 200 keV; these curves have been extrapolated to 1 MeV. The vertical lines show the indicated values of the electron energy, *T*.

Fig. 14. Ratio of IMFPs calculated from the relativistic TPP-2M equation [Eqns (26) and (29)] to IMFPs calculated from optical data as a function of electron energy for the 41 elemental solids.

Fig. 15. Comparison of IMFPs calculated from the relativistic optical-data model of Fernandez-Varea *et al*. [12] for Al, Si, Cu, and Au (solid squares) with our IMFPs (solid circles, Table 2) and IMFPs from the relativistic TPP-2M equation (solid lines, Eqns (26) and (29)) for energies between 10 eV and 200 keV.

Fig. 16. Comparison of IMFPs calculated from the relativistic optical-data model of Fernandez-Varea *et al*. [12] for Al, Si, Cu, and Au (solid squares) with our IMFPs (solid circles, Table 2) and IMFPs from the full version of the relativistic TPP-2M equation (solid lines, Eqns (25) and (29)) for energies between 100 keV and 1 MeV.

Fig. 17. Comparison of our calculated IMFPs at energies of 100 keV for 11 elemental solids and 200 keV for 32 elemental solids with the corresponding measured IMFPs [9,13-15]. The solid line indicates perfect correlation between the calculated

Author Manuscript:
Published in final edited form as: *Surf. Interface Anal*. Volume 47, Issue 9, Pages 871-888, September 2015. https://doi.org/10.1002/sia.5789

and measured IMFPs.

Fig. 18. Comparison of our IMFPs calculated from the relativistic TPP-2M equation [Eqns (26) and (29)] at energies of 100 keV for 11 elemental solids and 200 keV for 32 elemental solids with the corresponding measured IMFPs [9, 13-15]. The solid line indicates perfect correlation between the calculated and measured IMFPs.

Author Manuscript:
Published in final edited form as: *Surf. Interface Anal.* Volume 47, Issue 9, Pages 871-888, September 2015. https://doi.org/10.1002/sia.5789

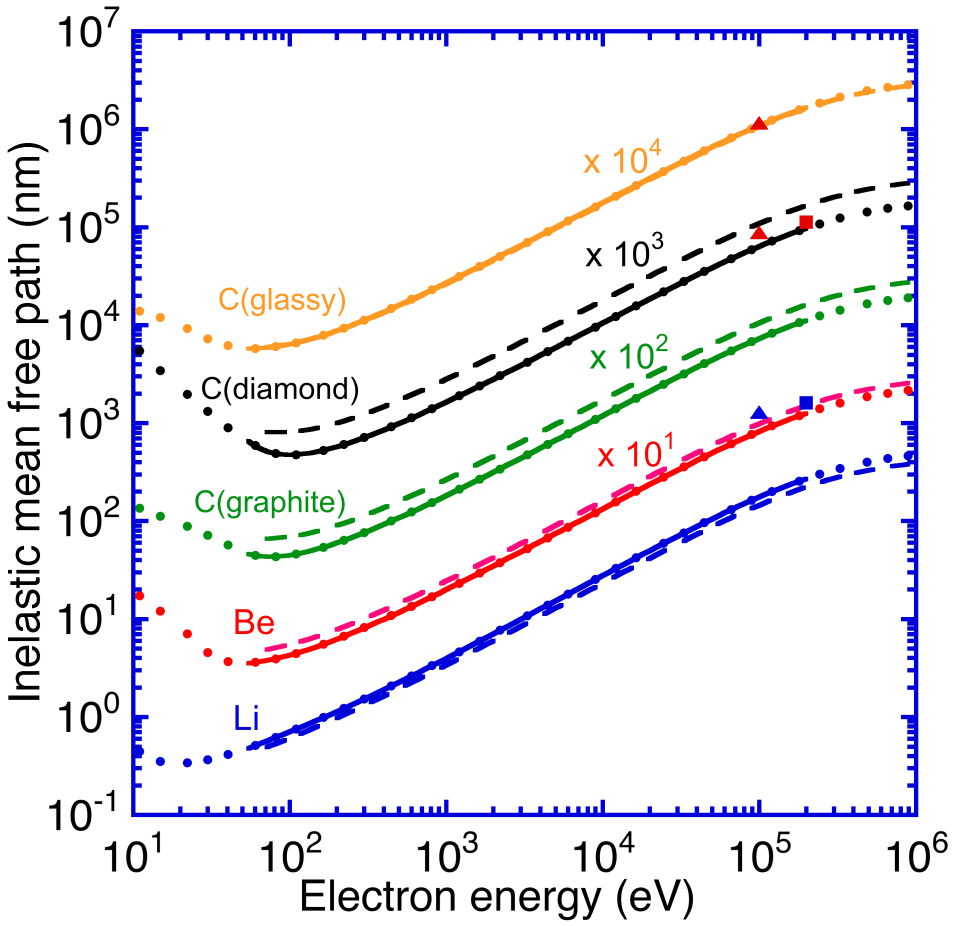

Fig. 1. Plots of calculated electron inelastic mean free paths as a function of relativistic electron kinetic energy for Li, Be, graphite, diamond, and glassy carbon. The solid circles show calculated IMFPs from the relativistic full Penn algorithm (Table 2). The solid lines show fits to these IMFPs with the relativistic modified Bethe equation [Eqn (26)] and the derived parameters in Table 3. The long-dashed lines indicate IMFPs calculated from the relativistic TPP-2M equation [Eqs. (26) and (29)]. The solid squares and triangles indicate IMFPs measured from TEM experiments at 200 keV by Iakoubovskii *et al.* [13] and from TEM experiments at 100 keV [9], respectively.

Author Manuscript:
Published in final edited form as: *Surf. Interface Anal.* Volume 47, Issue 9, Pages 871-888, September 2015. https://doi.org/10.1002/sia.5789

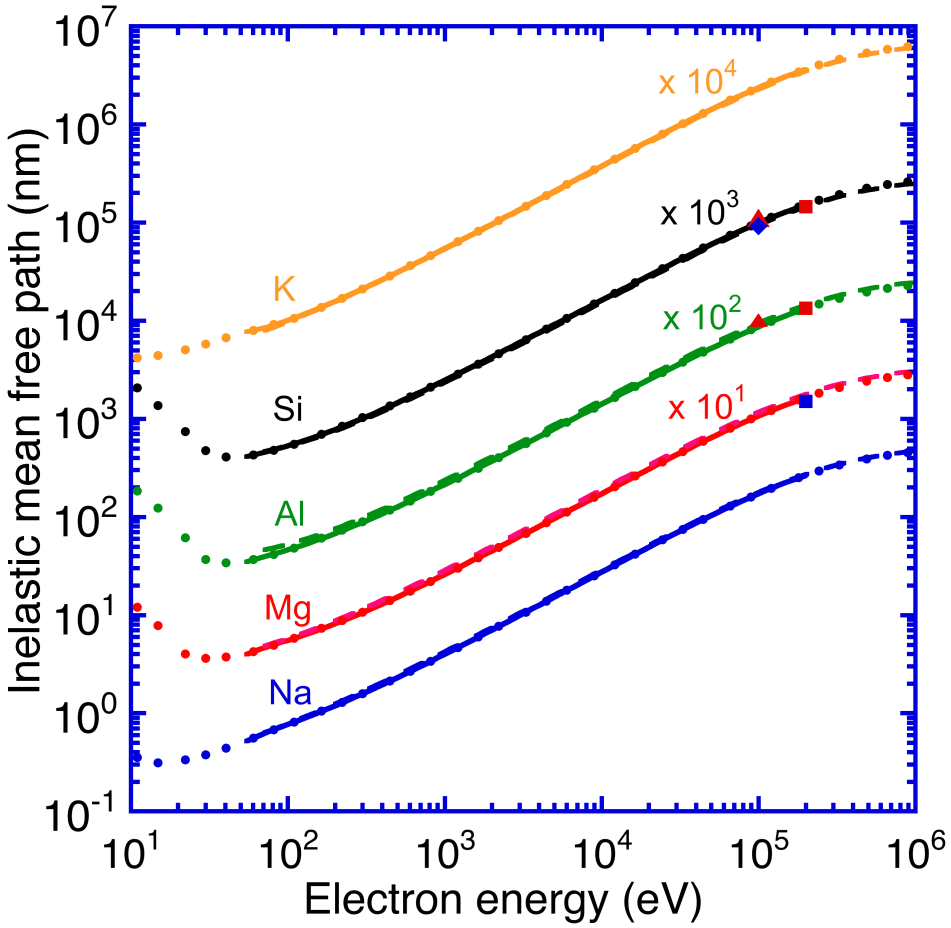

Fig. 2 Plots of calculated electron inelastic mean free paths as a function of relativistic electron kinetic energy for Na, Mg, Al, Si, and K. The solid diamond indicates an IMFP measured from TEM experiments for Si by McCartney *et al.* [14]. See caption to Fig. 1.

Author Manuscript:
Published in final edited form as: *Surf. Interface Anal.* Volume 47, Issue 9, Pages 871-888, September 2015. https://doi.org/10.1002/sia.5789

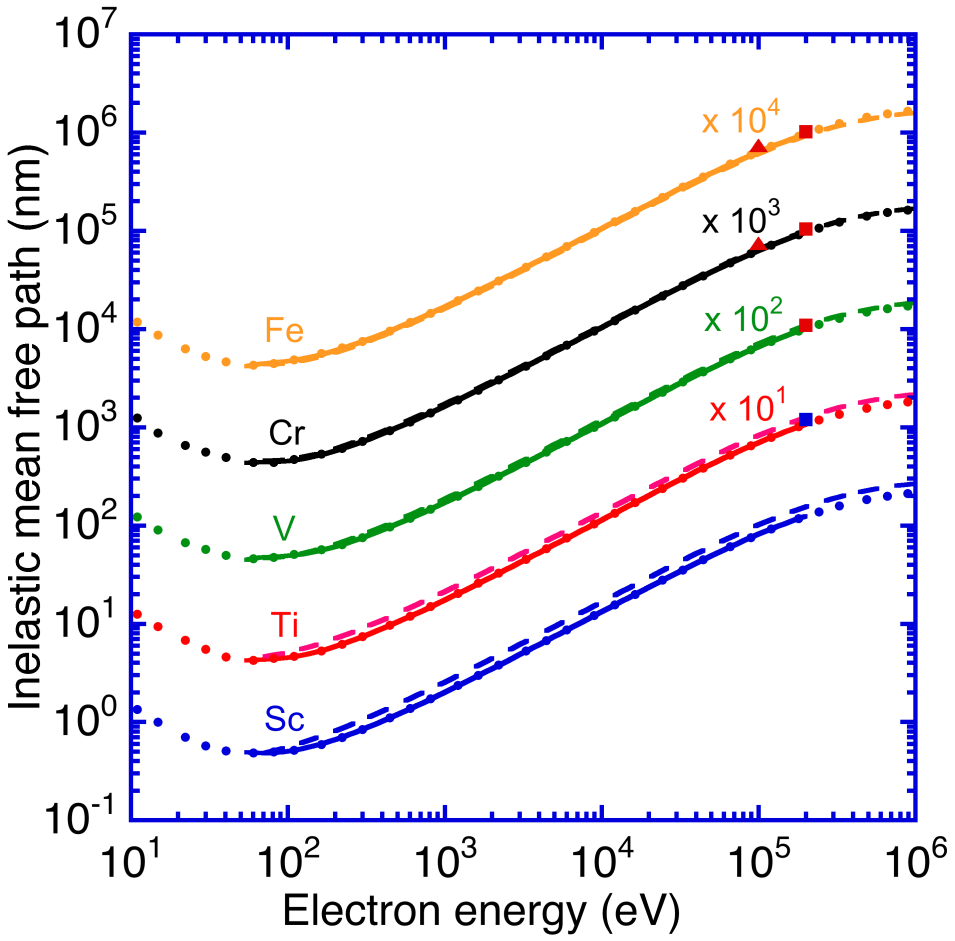

Fig. 3 Plots of calculated electron inelastic mean free paths as a function of relativistic electron kinetic energy for Sc, Ti, V, Cr, and Fe. See caption to Fig. 1.

Author Manuscript:
Published in final edited form as: *Surf. Interface Anal.* Volume 47, Issue 9, Pages 871-888, September 2015. https://doi.org/10.1002/sia.5789

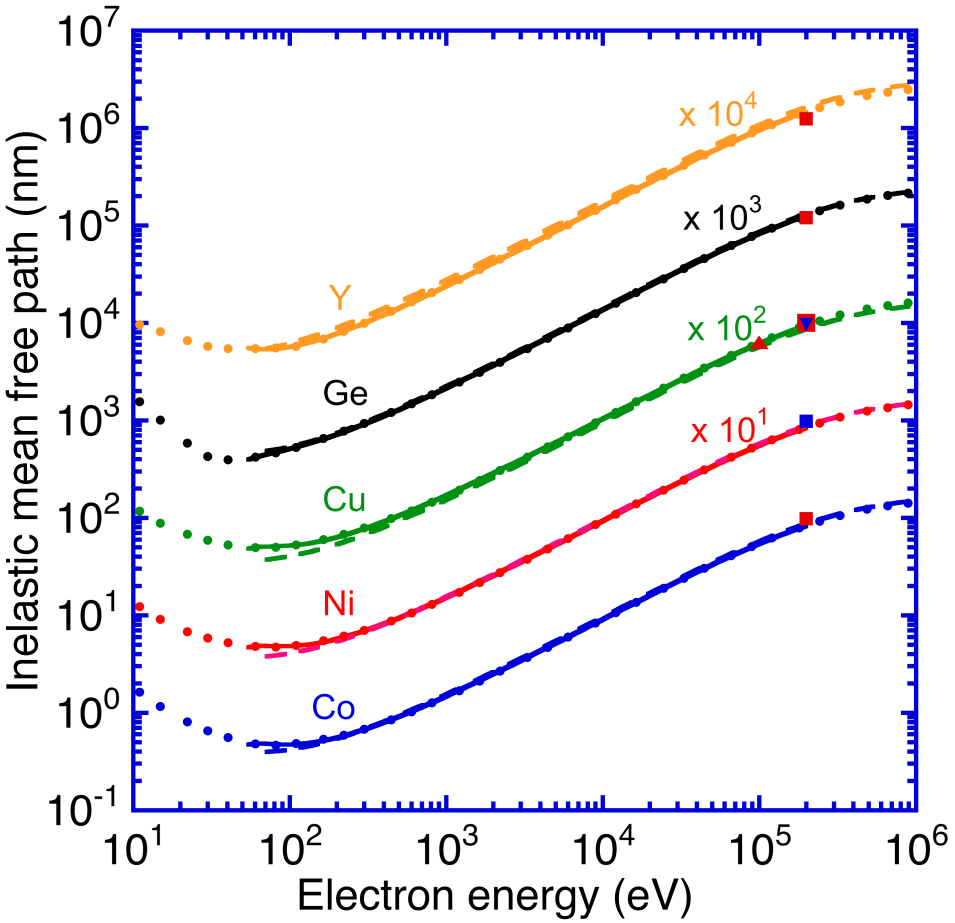

Fig. 4 Plots of calculated electron inelastic mean free paths as a function of relativistic electron kinetic energy for Co, Ni, Cu, Ge, and Y. The solid inverted triangle indicates an IMFP measured from TEM experiments for Cu by Wang *et al.* [15]. See caption to Fig. 1.

Author Manuscript:
Published in final edited form as: *Surf. Interface Anal*. Volume 47, Issue 9, Pages 871-888, September 2015. https://doi.org/10.1002/sia.5789

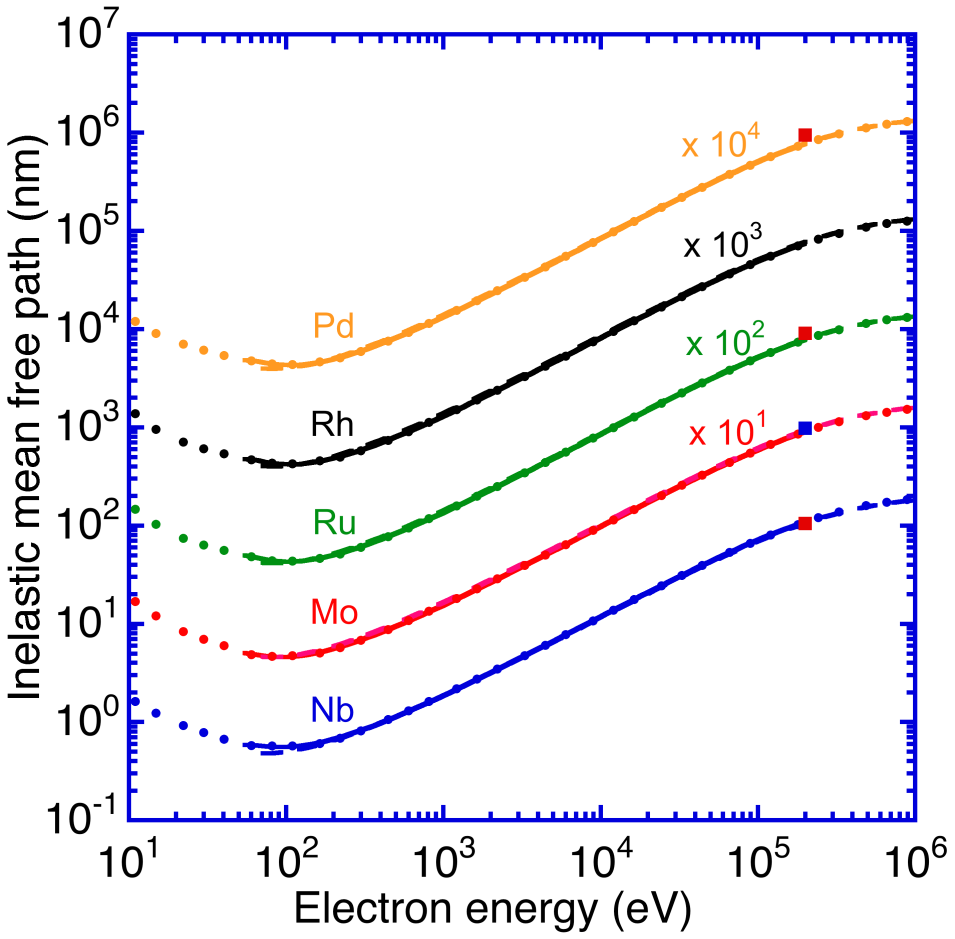

Fig. 5 Plots of calculated electron inelastic mean free paths as a function of relativistic electron kinetic energy for Nb, Mo, Ru, Rh, and Pd. See caption to Fig. 1.

Author Manuscript:
Published in final edited form as: *Surf. Interface Anal.* Volume 47, Issue 9, Pages 871-888, September 2015. https://doi.org/10.1002/sia.5789

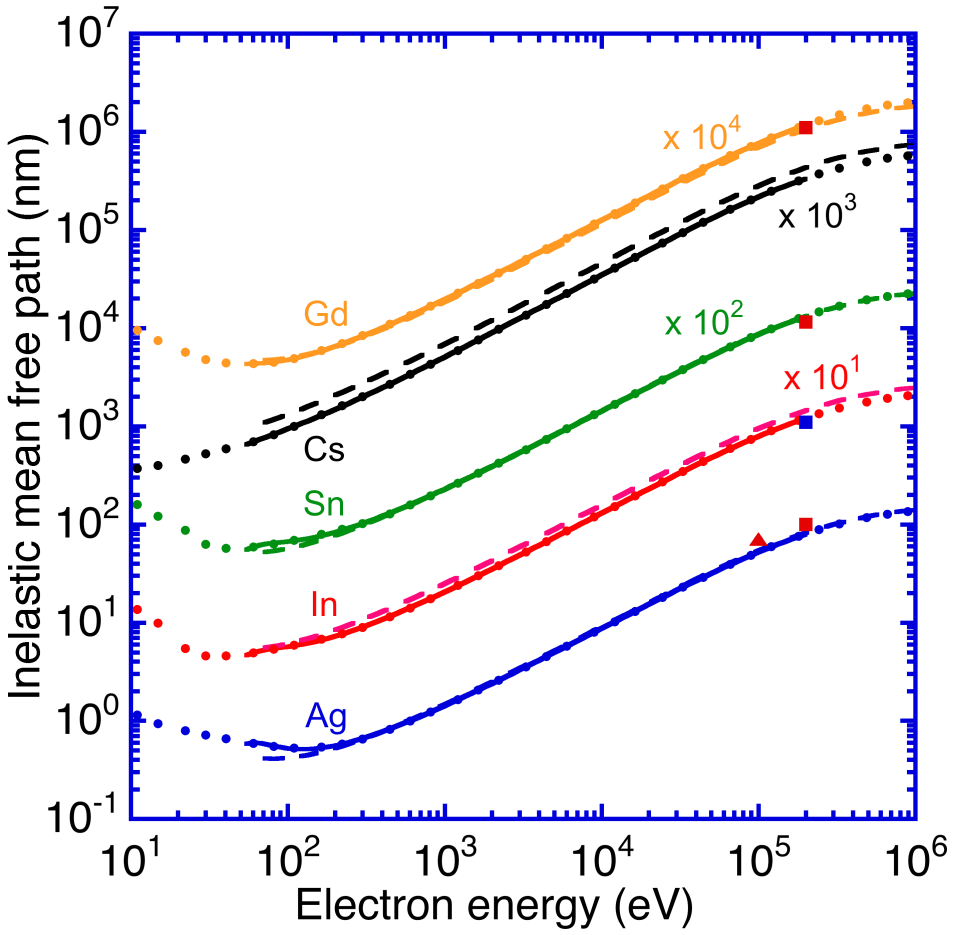

Fig. 6 Plots of calculated electron inelastic mean free paths as a function of relativistic electron kinetic energy for Ag, In, Sn, Cs, and Gd. See caption to Fig. 1.

Author Manuscript:
Published in final edited form as: *Surf. Interface Anal.* Volume 47, Issue 9, Pages 871-888, September 2015. https://doi.org/10.1002/sia.5789

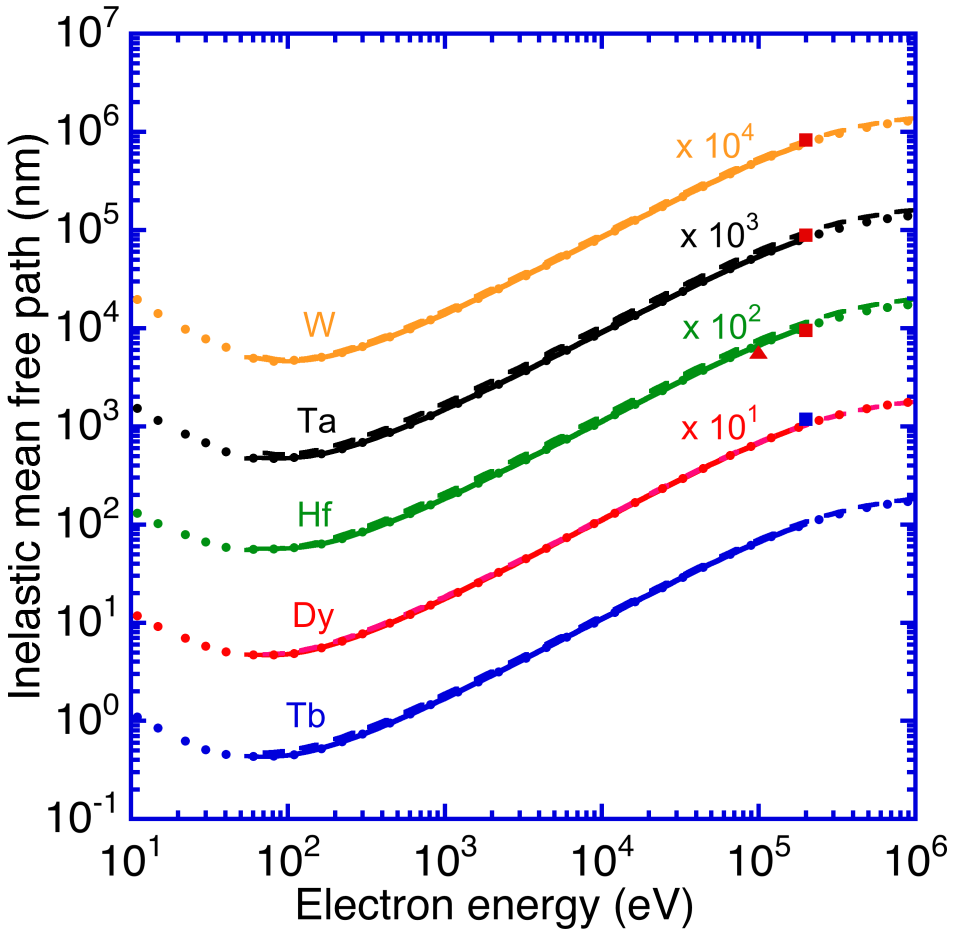

Fig. 7 Plots of calculated electron inelastic mean free paths as a function of relativistic electron kinetic energy for Tb, Dy, Hf, Ta, and W. See caption to Fig. 1.

Author Manuscript:
Published in final edited form as: *Surf. Interface Anal.* Volume 47, Issue 9, Pages 871-888, September 2015. https://doi.org/10.1002/sia.5789

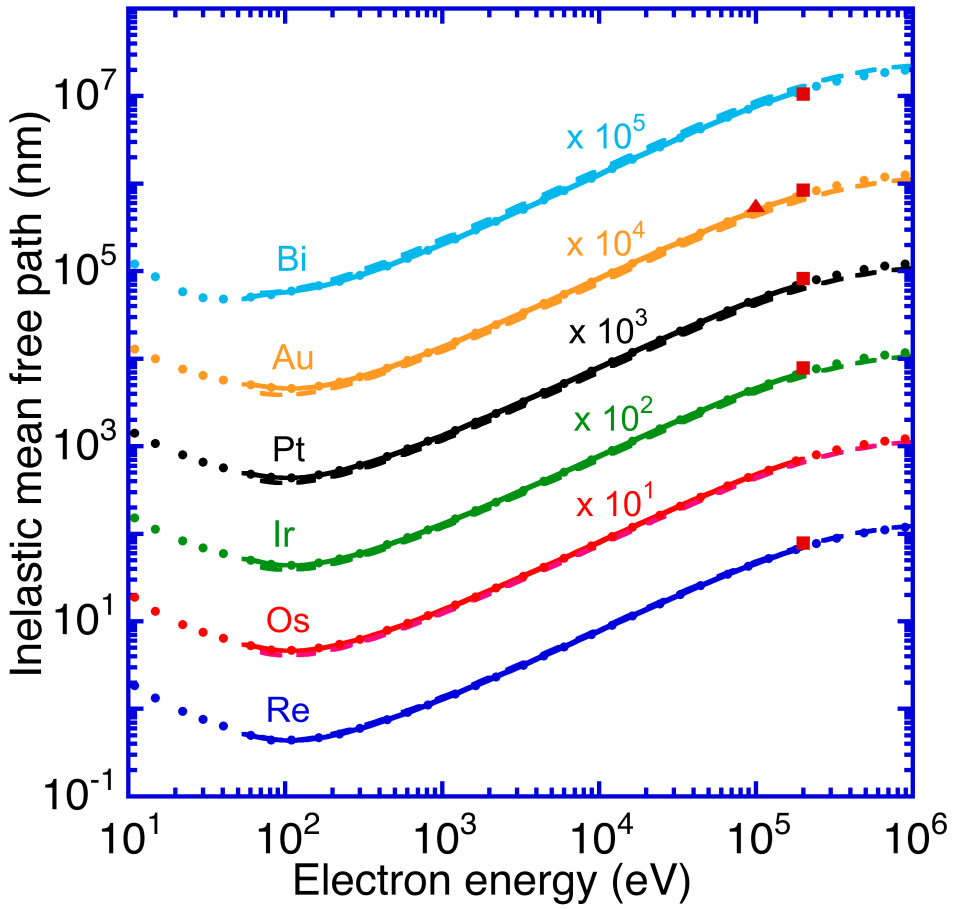

Fig. 8 Plots of calculated electron inelastic mean free paths as a function of relativistic electron kinetic energy for Re, Os, Ir, Pt, Au, and Bi. See caption to Fig. 1.

Author Manuscript:
Published in final edited form as: *Surf. Interface Anal.* Volume 47, Issue 9, Pages 871-888, September 2015. https://doi.org/10.1002/sia.5789

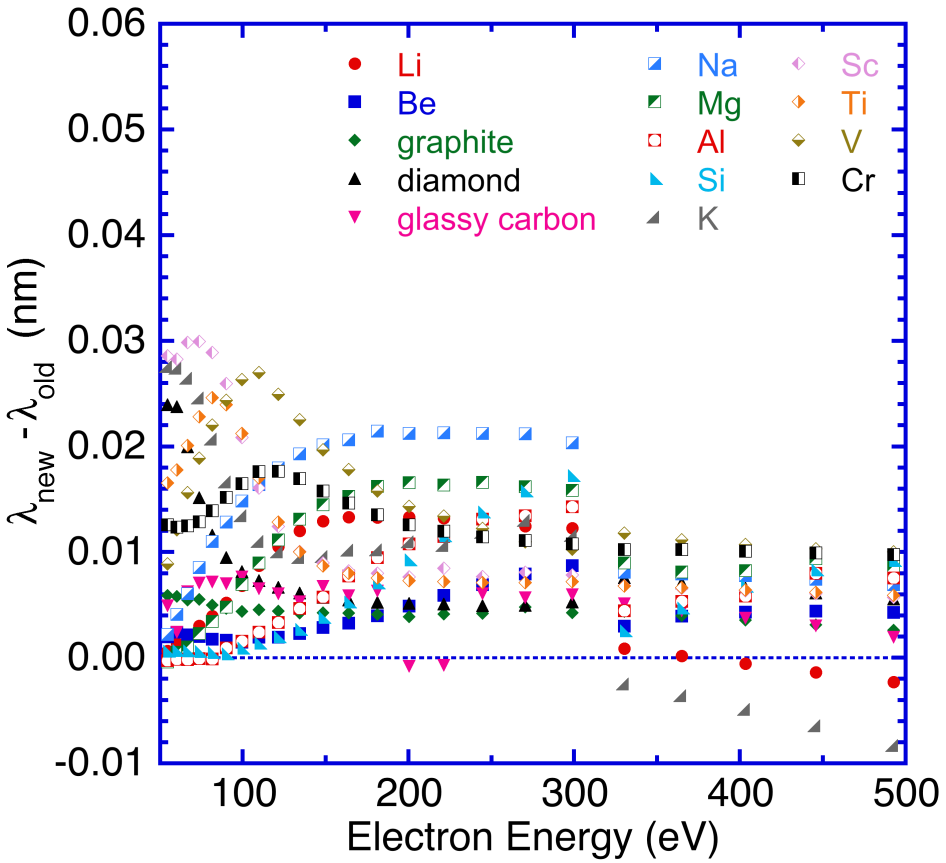

Fig. 9. Plots of the differences between the IMFPs in Table 2 for Li, Be, graphite, diamond, glassy carbon, Na, Mg, Al, Si, K, Sc, Ti, V, and Cr that were calculated with the newer procedure for triple integrals with the FPA (λ_{new}) and the corresponding IMFPs that were published previously (λ_{old}) in Ref. 8 as a function of electron energy.

Author Manuscript:
Published in final edited form as: *Surf. Interface Anal.* Volume 47, Issue 9, Pages 871-888, September 2015. https://doi.org/10.1002/sia.5789

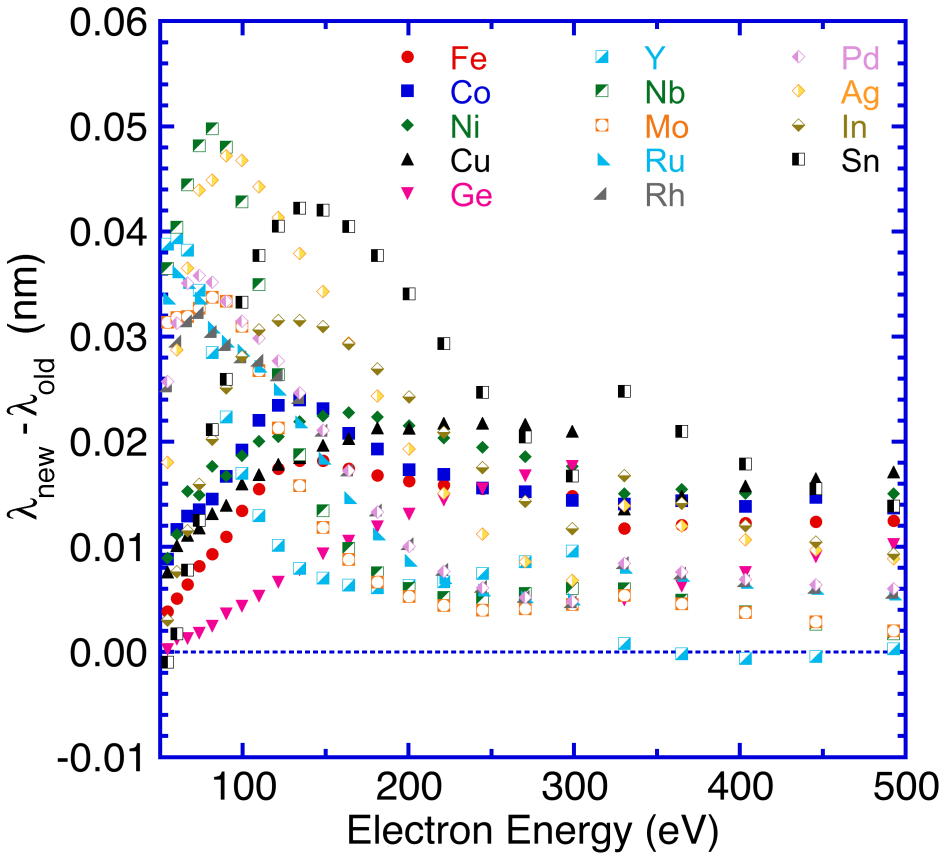

Fig. 10. Plots of the differences between λ_{new} and λ_{old} as a function of electron energy for Fe, Co, Ni, Cu, Ge, Y, Nb, Mo, Ru, Rh, Pd, Ag, In, and Sn. See caption to Fig. 9.

Author Manuscript:
Published in final edited form as: *Surf. Interface Anal.* Volume 47, Issue 9, Pages 871-888, September 2015. https://doi.org/10.1002/sia.5789

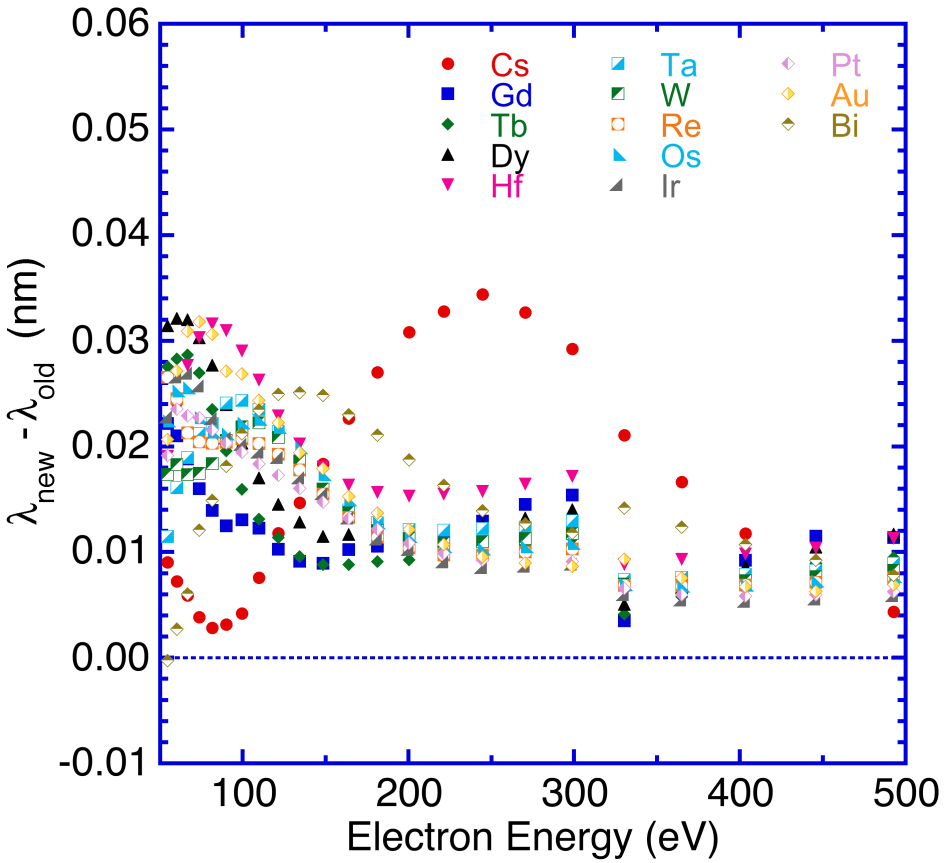

Fig. 11. Plots of the differences between λ_{new} and λ_{old} as a function of electron energy for Cs, Gd, Tb, Dy, Hf, Ta, W, Re, Os, Ir, Pt, Au, and Bi. See caption to Fig. 9.

Author Manuscript:
Published in final edited form as: *Surf. Interface Anal*. Volume 47, Issue 9, Pages 871-888, September 2015. https://doi.org/10.1002/sia.5789

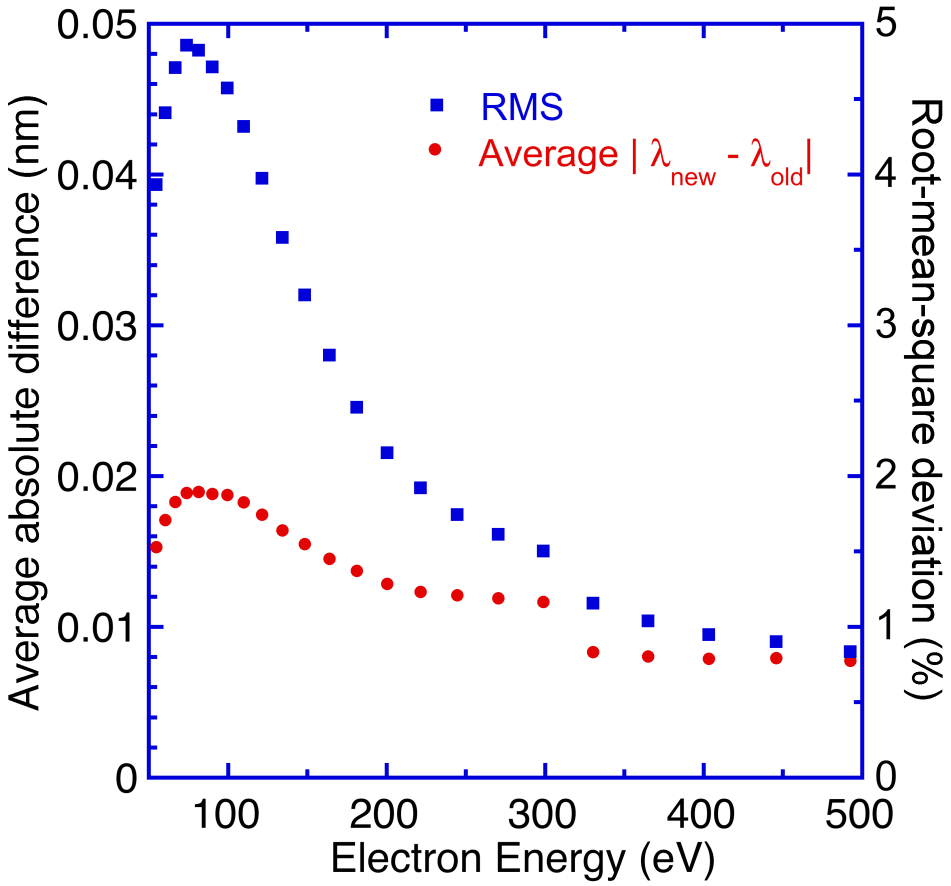

Fig. 12. Plots of the average absolute differences [$= \sum |\lambda_{new} - \lambda_{old}| / n$] and of the percentage root-mean-square deviations [$= 100 \sum \{(\lambda_{new} - \lambda_{old}) / \lambda_{old}\} / n$] as a function of electron energy for the 41 elemental solids.

Author Manuscript:
Published in final edited form as: *Surf. Interface Anal.* Volume 47, Issue 9, Pages 871-888, September 2015. https://doi.org/10.1002/sia.5789

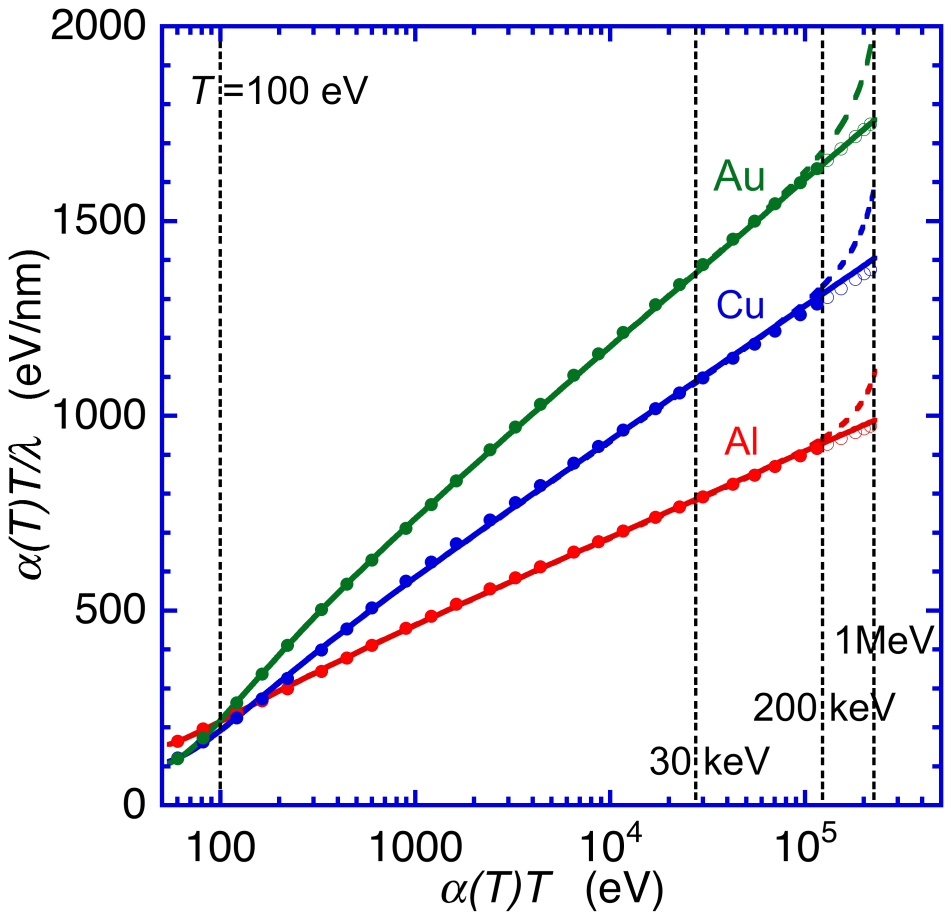

Fig. 13. Fano plots for Al, Cu, and Au based on Eqn (26). The solid and open circles represent IMFPs calculated with the relativistic FPA. The solid and dashed lines show curve-fit results with Eqns (26) and (25), respectively, for energies between 50 eV and 200 keV; these curves have been extrapolated to 1 MeV. The vertical lines show the indicated values of the electron energy, T.

Author Manuscript:
Published in final edited form as: *Surf. Interface Anal*. Volume 47, Issue 9, Pages 871-888, September 2015. https://doi.org/10.1002/sia.5789

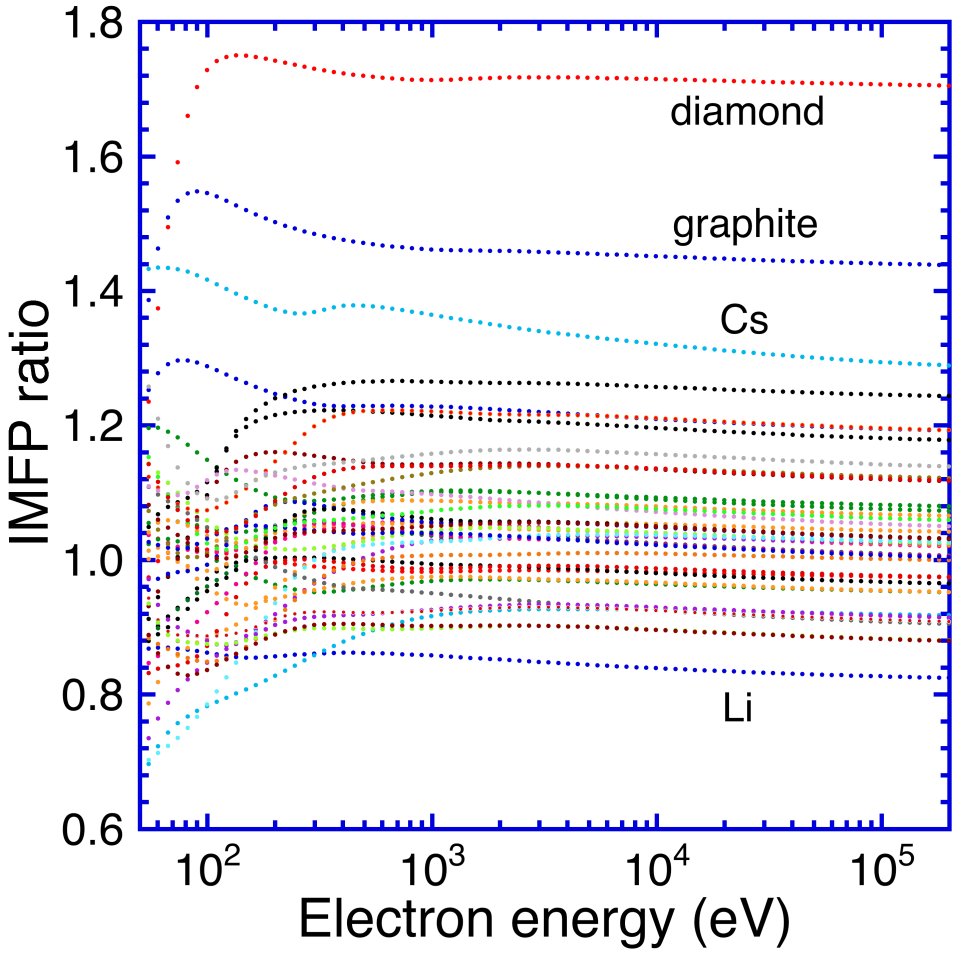

Fig. 14. Ratio of IMFPs calculated from the relativistic TPP-2M equation [Eqns (26) and (29)] to IMFPs calculated from optical data as a function of electron energy for the 41 elemental solids.

Author Manuscript:
Published in final edited form as: *Surf. Interface Anal.* Volume 47, Issue 9, Pages 871-888, September 2015. https://doi.org/10.1002/sia.5789

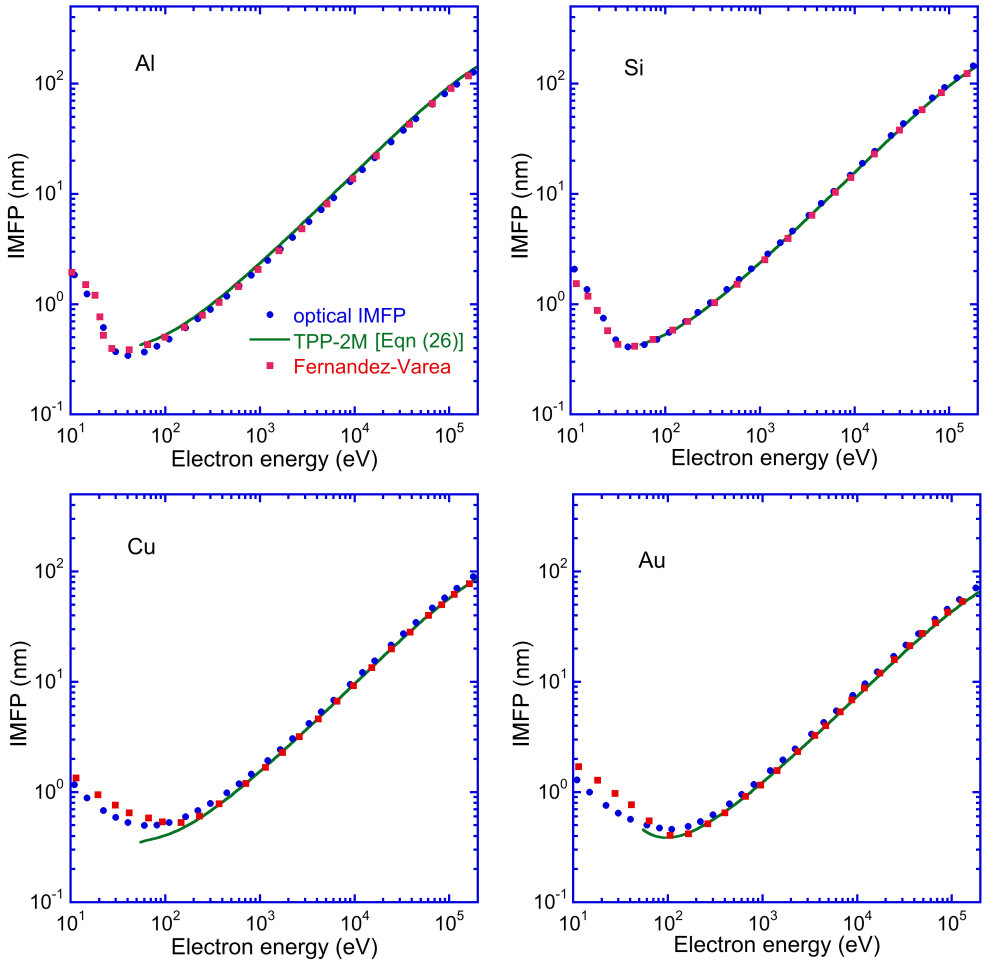

Fig. 15. Comparison of IMFPs calculated from the relativistic optical-data model of Fernandez-Varea *et al*. [12] for Al, Si, Cu, and Au (solid squares) with our IMFPs (solid circles, Table 2) and IMFPs from the relativistic TPP-2M equation (solid lines, Eqns (26) and (29)) for energies between 10 eV and 200 keV.

Author Manuscript:
Published in final edited form as: *Surf. Interface Anal.* Volume 47, Issue 9, Pages 871-888, September 2015. https://doi.org/10.1002/sia.5789

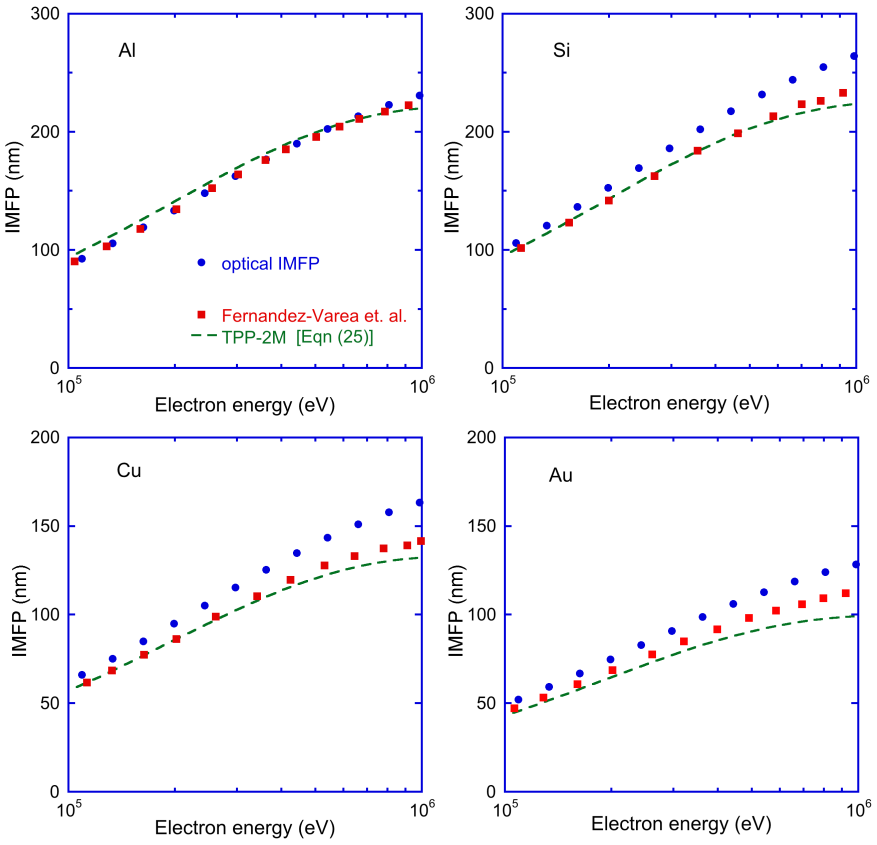

Fig. 16. Comparison of IMFPs calculated from the relativistic optical-data model of Fernandez-Varea *et al*. [12] for Al, Si, Cu, and Au (solid squares) with our IMFPs (solid circles, Table 2) and IMFPs from the full version of the relativistic TPP-2M equation (solid lines, Eqns (25) and (29)) for energies between 100 keV and 1 MeV.

Author Manuscript:
Published in final edited form as: *Surf. Interface Anal*. Volume 47, Issue 9, Pages 871-888, September 2015. https://doi.org/10.1002/sia.5789

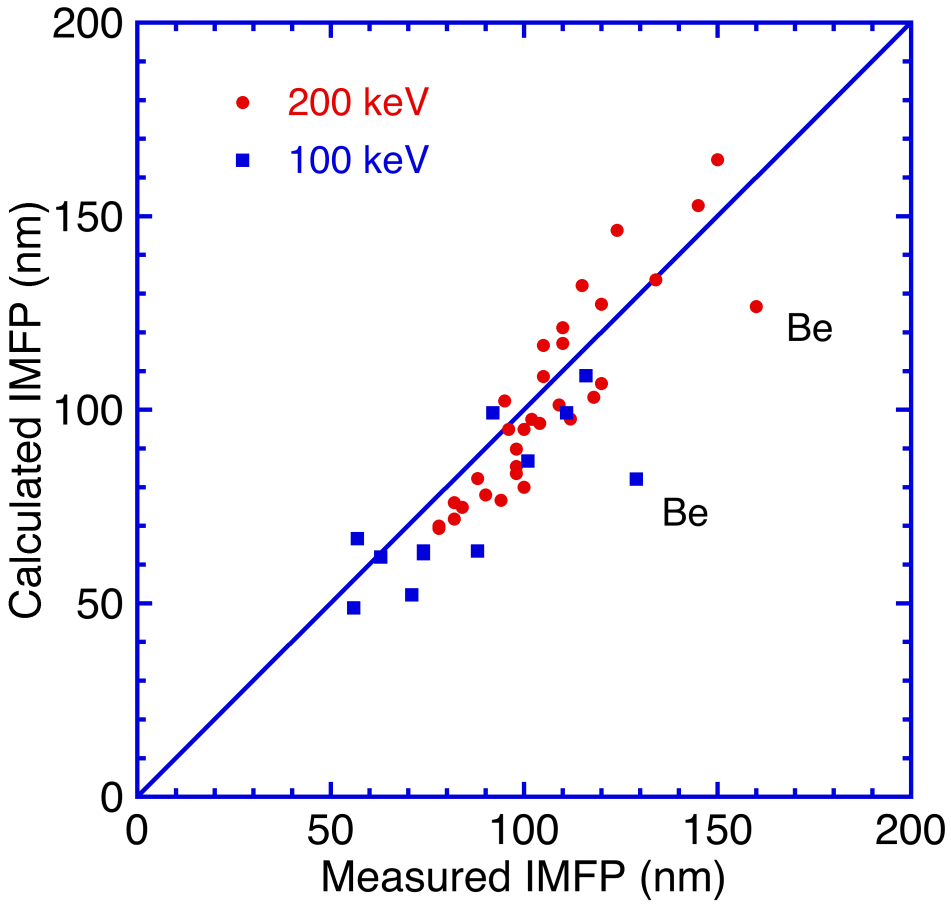

Fig. 17. Comparison of our calculated IMFPs at energies of 100 keV for 11 elemental solids and 200 keV for 32 elemental solids with the corresponding measured IMFPs [9,13-15]. The solid line indicates perfect correlation between the calculated and measured IMFPs.

Author Manuscript:
Published in final edited form as: *Surf. Interface Anal.* Volume 47, Issue 9, Pages 871-888, September 2015. https://doi.org/10.1002/sia.5789

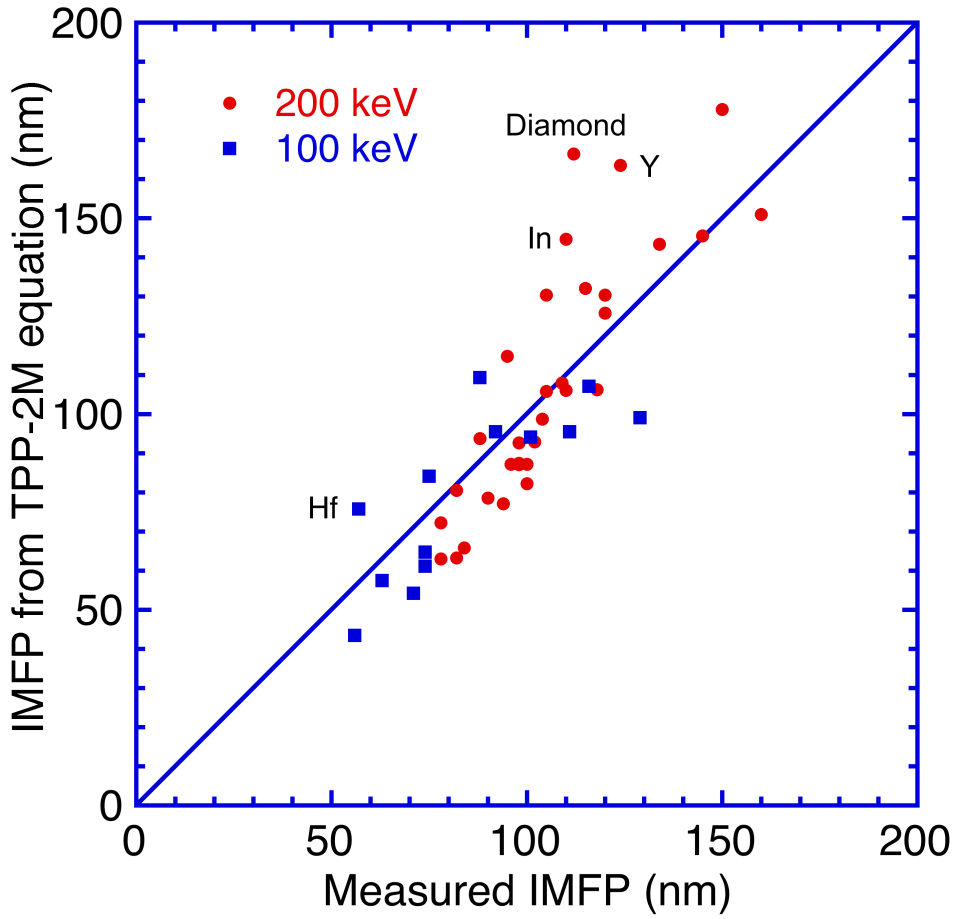

Fig. 18. Comparison of our IMFPs calculated from the relativistic TPP-2M equation [Eqns (26) and (29)] at energies of 100 keV for 11 elemental solids and 200 keV for 32 elemental solids with the corresponding measured IMFPs [9, 13-15]. The solid line indicates perfect correlation between the calculated and measured IMFPs.